

Article

Modeling and Test Results of an Innovative Gyroscope Wave Energy Converter

Zhongcai Pei, Hao Jing  and Zhiyong Tang * 

School of Automation Science and Electrical Engineering, Beihang University, Beijing 100191, China; peizc@buaa.edu.cn (Z.P.); jinghao@buaa.edu.cn (H.J.)

* Correspondence: zyt_76@buaa.edu.cn; Tel.: +86-15646500578

Abstract: An improved Maximum Power Point Tracking (MPPT) method based on a purely mechanical wave energy converter (WEC) of gyroscope precession is proposed. The method adopts dynamic perturbation step adjustment, which improves the stability of power output and reduces steady-state oscillation. The paper introduces the principle of the device, establishes the mathematical model, and obtains the complete expression of power. The effect of wave frequency, pitch amplitude, power take-off (PTO) damping coefficient, and flywheel rotating speed on power output is analyzed. The output regression equation is established, and the extraction conditions of the maximum power are summarized and predicted. Aiming at the time-varying nature of actual ocean waves, a variable step size modified maximum power point (MPP) tracking control algorithm based on perturbation and observation (P&O) method is proposed. The algorithm has a unique technology to dynamically change the perturbation size, which not only improves the dynamic response but also reduces the oscillation. Besides, the boundary conditions ensure that the algorithm will not deviate from the motion trajectory, and the average filtering method and steady-state judgment can further reduce steady-state oscillation. In various ocean conditions, the proposed method has better output stability compared with other variable step size algorithms. Finally, different wave working conditions are given in the experiment, and the results verify the effectiveness of the proposed MPPT control strategy in experimental equipment. The device will be suitable for distributed power sources in small islands and ports.

Keywords: gyroscopic power take-off; wave energy converter (WEC); wave power; maximum power point (MPP) tracking (MPPT); modified adaptive perturb and observe (P&O)



Citation: Pei, Z.; Jing, H.; Tang, Z. Modeling and Test Results of an Innovative Gyroscope Wave Energy Converter. *Appl. Sci.* **2021**, *11*, 4359. <https://doi.org/10.3390/app11104359>

Academic Editor: Tomonobu Senjyu

Received: 14 April 2021

Accepted: 8 May 2021

Published: 11 May 2021

Publisher's Note: MDPI stays neutral with regard to jurisdictional claims in published maps and institutional affiliations.



Copyright: © 2021 by the authors. Licensee MDPI, Basel, Switzerland. This article is an open access article distributed under the terms and conditions of the Creative Commons Attribution (CC BY) license (<https://creativecommons.org/licenses/by/4.0/>).

1. Introduction

In the past few decades, the entire world has lived in a great crisis of energy shortage and the deterioration of the environment [1]. With the decline in fossil resources, the use of renewable energy solves one of the major concerns of the world community [2]. Clean and renewable energy technologies making use of ocean energy provide us with pollution-free alternatives to fossil fuel power plants and serve as a response to global warming and growing electricity demand. The oceans supply many kinds of renewable energy, such as ocean thermal energy conversion, marine current power, salinity gradient power, and eventually wave power [3,4]. Among all these ocean energy resources, wave energy is receiving growing attention because of its enormous potential energy [5].

Various types of wave energy converters (WECs) have been invented so far to extract energy from ocean waves to develop wave energy [6]. Although, after over 40 years of effort, wave energy still remains in the research and prototype stages, with only a few pilot plants connected to the grid worldwide [7,8]. The current main energy conversion methods can be divided into three main types. Take Wave Dragon [9] and Tapchan [10] for example; the first kind uses potential energy stored in reservoirs, and the principle is basically the same as that of hydropower dams. The second is to compress the medium

based on the relative movement between the components, such as the oscillating water column. The third type uses a high-speed rotating rotor to store a substantial amount of energy as kinetic energy (flywheel effect—the Wells turbine) [11]. In all kinds of WECs, point absorbers [12,13], oscillating water columns [14,15], and flaps [16] have become the most common devices in the wave energy field.

However, some issues still need to be resolved, such as the survivability of the equipment, environmental pollution (if a hydraulic conversion system is used), the economics of energy extraction, and power output stability [17,18]. The WECs work in extreme environments, for example, Toftesfallen, Norway, built equipment in 1985, but it was severely damaged in 1991, which means higher technical requirements and a more advanced structure. Since then, researchers have made a lot of attempts, but still cannot avoid the damage of WECs. The most famous is the Aguçadoura wave farm in Portugal, the first wave farm in the world that integrated three types of Pelamis equipment, which stopped its operation after two months [19]. Besides, in hydraulically driven WECs, hydraulic oil leakage caused by loss of lubrication, wear, and other factors will cause irreversible damage to the marine environment [20].

According to the global wave energy atlas proposed by Konet [21], deep waters (40° – 60° N and 40° – 60° S) have abundant wave energy resources (70 kW/m) [22], and the energy density will decrease as the waves approach the coast, so it is appropriate to install WECs in deep water. However, one of the shortcomings of these devices is that the areas with high wave energy density are far away from the power grid, thus increasing the proportion of cable installation and maintenance costs in the investment of water conservancy projects and increasing commercial costs. From the economic point of view, the nearshore wave energy resources cannot be ignored, because the shallower waters and islands associated with the nearshore are critical to the operation and economic costs of certain WECs [23]. Japan does not have a substantial amount of wave power, but a WEC was developed successfully in the full-scale test [24]. Therefore, the current wave energy development and test power stations are mainly related to the coastal waters, and the development of small-scale wave energy has become a research hotspot in some coastal countries [25].

Therefore, in recent years, nearshore enclosed WECs have become more popular with the conversion systems not in contact with water [26,27]. The main advantage is that there are no moving parts in the water with survivability, and the purely mechanical device is friendly to the ocean. The University of Rome has developed a new type of wave energy device, which is especially suitable for enclosed sea areas with moderate wave power [4]. Kobe University applied the gyroscope principle to extract wave energy in the low-energy density ocean and successfully developed a 5.5 kW WEC in 2003 [28]. The gyroscope principle is used by the above two WECs to convert wave energy into electricity. Compared with other WECs with different structures or conversion principles, these WECs have the advantages of high reliability, low construction and maintenance costs, and easy implementation of active control strategies [29].

The design of WEC is quite different in the method of energy extraction, but all of them require a core of the WEC, called the power take-off (PTO) system, to convert the mechanical motion of the primary wave interface into a stable energy output. Additionally, there is an optimal damping point under different sea conditions for the PTO system, so the PTO can be controlled by the maximum power point (MPP) tracking (MPPT) control algorithms to improve the generated power of the system [30]. MPPT is an adaptive control strategy, which has been widely used in renewable energy such as wind and solar energy [31]. In the application of renewable energy, the duty cycle of the voltage converter is usually applied to adjust the load resistance in the generator. At present, MPPT methods are mainly divided into two categories, namely conventional methods and soft computing methods. The methods based on software calculations such as artificial neural networks, fuzzy algorithms, and particle swarm algorithms have excellent steady-state performance but have not been widely recognized due to their slow calculation speed. The conventional

algorithms are perturb and observe (P&O) and incremental conductance, especially P&O, which is the most extensively used due to its simplicity and low cost [32,33].

However, there are two main problems with these methods. Firstly, the MPPT controller occasionally makes the system deviate from the optimal operating point when the external conditions change rapidly. Another disadvantage is that when the MPP is approached, the system will continuously oscillate around the MPP [34]. One of the most significant parameters of P&O is the length of perturbation. A smaller value will result in slower tracking performance and poor dynamic response, while a larger one will cause steady-state oscillation and energy waste [35]. Therefore, the adjustable perturbation step size can simultaneously meet the system's requirements for dynamic tracking and steady-state characteristics. Several MPPT techniques have been investigated for creating adaptive perturbing step size to enhance MPPT control [36], but these methods are limited to specific conditions [37–39]. Therefore, solving the two shortcomings has become the key to improving the P&O method.

Compared with other structures of WEC, this paper creatively develops a compact, high-safety, and non-polluting purely mechanical wave power generation system. It is anchored underwater and can be lowered to the seabed in extreme ocean conditions, thereby avoiding potential damage near the sea surface. The high-speed rotating flywheel is sealed in a float. When activated by external waves, it proceeds to generate electricity due to the gyroscope principle. This design reduces the energy conversion process and is sensitive to external excitations so that a wider range of waves can be captured. The main work of this paper is as follows. Firstly, the principle of gyroscope WEC is introduced in Section 2 and the mathematical model of the precession torque is established by MATLAB in Section 3. Secondly, the physical model and test environment are introduced in detail, including the various components of the gyroscope and the composition of the test platform, in Section 4. In Section 5, the influence of each input parameter on the power is obtained, and the complete expression of the output is obtained through linear regression and prediction. In Section 6, a modified MPPT algorithm is proposed to test the performance of the system, including a variable step size algorithm, reducing the steady-state error and the application of filters. After that, the performance of the proposed algorithm under different sea conditions is tested and compared with the other two variable step size P&O algorithms in Section 7.2. The results show that the proposed algorithm has excellent stability and good rapidity in various sea conditions. Finally, in Section 7.3, the model is verified through experimental testing, finding a reasonable agreement between simulation and experimental results.

2. Principle of System

The gyroscope principle is applied to convert the undulating wave energy into the gyroscope precession torque. The reference frames are used to analyze the movement of the system in Figure 1. The moving coordinate system $x_1y_1z_1$ is obtained by the fixed coordinate system XYZ through two rotating angular velocities $\dot{\delta}$ and $\dot{\epsilon}$. In the initial position without wave excitation, the moving coordinate system coincides with the fixed coordinate system, where $\dot{\delta} = 0$ and $\dot{\epsilon} = 0$, and the flywheel rotates at a constant velocity $\dot{\varphi}$ along the Z -axis. If the torque applied by the external waves is along the X -axis, the gyroscope's rotating angular velocity direction and the wave torque acting direction are perpendicular to each other. The flywheel is affected by two angular velocities $\dot{\varphi}$ and $\dot{\delta}$, and the gyroscopic effect produces a torque on the direction y_1 , which is perpendicular to the two velocities. By driving the gear to increase the angular velocity of precession, and driving the rotating PTO to generate energy, then the energy is converted from the wave to electric energy. But if the flywheel rotates in the direction of the wave (X -axis), the two angular velocities coincide and no power will be generated.

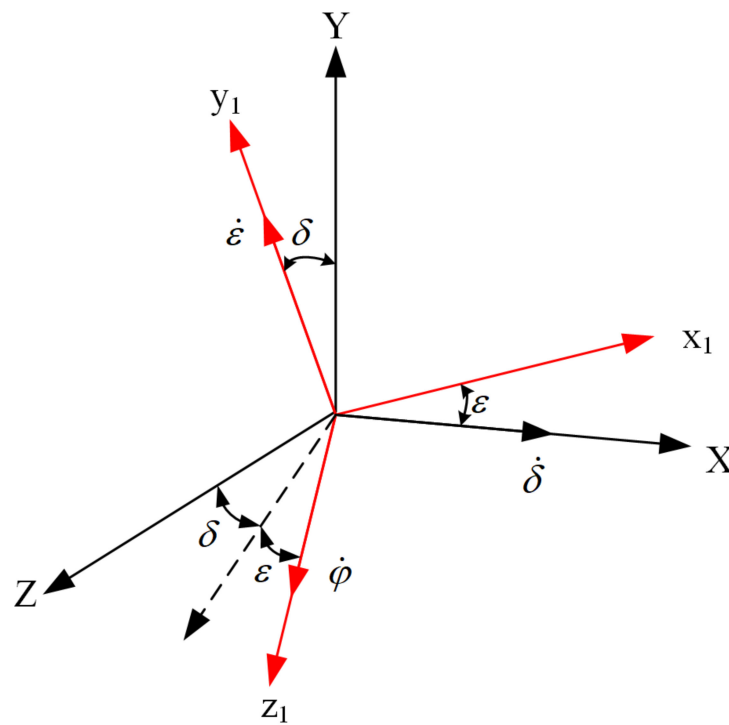


Figure 1. Reference frames.

The functional layout of the gyroscope wave energy converter (GWEC) is presented in Figure 2. The gyroscope device is sealed in the float, and the monitor must be connected to the system to obtain real-time power and efficiency. In this case, the gyroscope is considered to be a motor on the damper, and the system extracts the energy of the damper for power generation in the PTO. The damper can be directly connected to the generator on the Y-axis. In this paper, the damping is connected to the monitor to verify the prototype performance, and the prototype will produce gyroscope torque, regardless of whether it contains external damping.

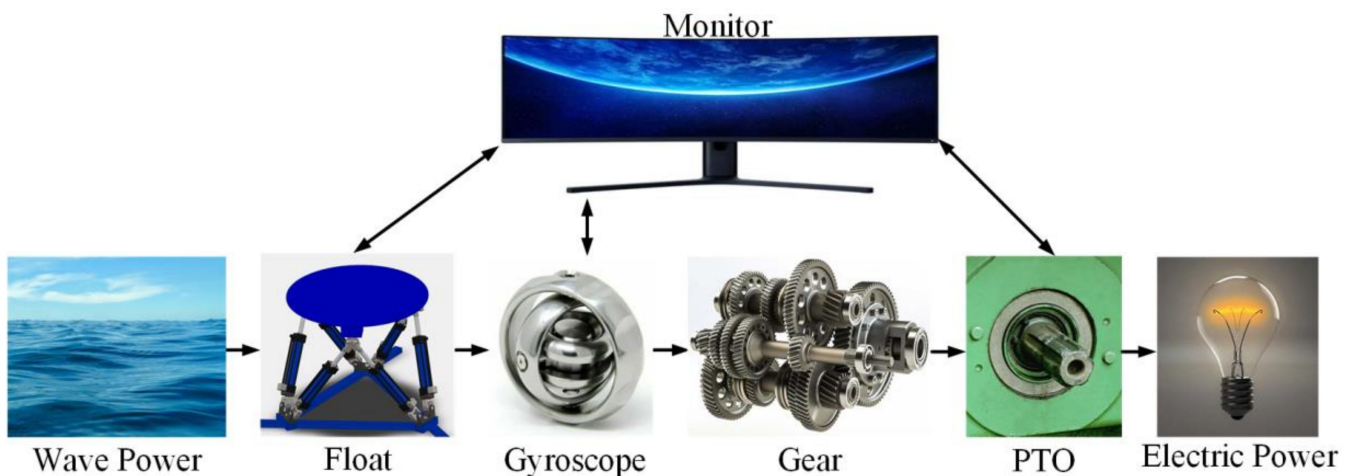


Figure 2. Principle of GWEC.

3. Theoretical Analysis

Assuming that the gyroscope rotor rotates about the Z-axis at an angular velocity $\dot{\varphi}$, the floating platform and the flywheel both rotate around the X-axis at an angular velocity $\dot{\delta}$ by the motion of the wave. Then, the flywheel coordinate system is used as the moving

coordinate system (the unit vector of the moving coordinate system is $\vec{i}, \vec{j}, \vec{k}$ respectively), the angular velocity of the gyroscope rotor relative to the inertial space is:

$$\vec{\omega} = \dot{\delta} \cos \varepsilon \cdot \vec{i} + \dot{\varepsilon} \cdot \vec{j} + (\dot{\delta} \sin \varepsilon + \dot{\varphi}) \cdot \vec{k} \tag{1}$$

where ε is the gyroscope precession angle. Then, the angular momentum of the rotor can be obtained (where J_x, J_y, J_z are the moments of inertia in x, y, z directions).

$$H = J_x \dot{\delta} \cos \varepsilon \cdot \vec{i} + J_y \dot{\varepsilon} \cdot \vec{j} + J_z (\dot{\delta} \sin \varepsilon + \dot{\varphi}) \cdot \vec{k} \tag{2}$$

The change of the precession angle is the key to wave energy generation. According to the expression of angular momentum, the equation of motion of the y_1 is written:

$$J_y \ddot{\varepsilon} + (J_x - J_z) \dot{\delta}^2 \sin \varepsilon \cos \varepsilon - J_z \dot{\varphi} \dot{\delta} \cos \varepsilon = T_y \tag{3}$$

where T_y is the control torque in the direction of the precession axis, the PTO can be considered as a spring damping system, and Equation (3) can be rewritten as:

$$J_y \ddot{\varepsilon} + (J_x - J_z) \dot{\delta}^2 \sin \varepsilon \cos \varepsilon - J_z \dot{\varphi} \dot{\delta} \cos \varepsilon = -c_y \dot{\varepsilon} - k_y \varepsilon \tag{4}$$

where c_y is the damping coefficient and k_y is the spring coefficient. When ε is small, $\sin \varepsilon$ is approximately equal to 0. It can be noticed in Equation (4) that the second term of the above formula is two orders of magnitude smaller than the others, so it can be ignored to reduce the amount of calculation. Then, Equation (4) can be rewritten as follows:

$$J_y \ddot{\varepsilon} + c_y \dot{\varepsilon} + k_y \varepsilon = J_z \dot{\varphi} \dot{\delta} \cos \varepsilon \tag{5}$$

In order to obtain the main behavioral characteristics and dynamic performance of the gyroscope device, Equation (5) has been linearized around the position ε approximately equal to 0.

$$J_y \ddot{\varepsilon} + c_y \dot{\varepsilon} + k_y \varepsilon = J_z \dot{\varphi} \dot{\delta} \tag{6}$$

It can be observed that Equation (6) is a typical second-order system, which can be rewritten as:

$$\ddot{\varepsilon} + 2\zeta \omega_n \dot{\varepsilon} + \omega_n^2 \varepsilon = J_z \dot{\varphi} \dot{\delta} / J_y \tag{7}$$

where equivalent damping ratio $\zeta = \frac{c_y}{2\sqrt{J_y k_y}}$, free oscillation frequency $\omega_n = \sqrt{\frac{k_y}{J_y}}$. When a certain input $\dot{\delta}$ is given to the system, we can observe the output as:

$$(-J_y \omega^2 \sin(\omega t) + c_y \omega \cos(\omega t) + k_y \sin(\omega t)) \varepsilon_0 = J_z \dot{\varphi} \dot{\delta} \tag{8}$$

where ω is the frequency of the wave, $\varepsilon = \varepsilon_0 \sin(\omega t)$ by assuming the gyroscope precession change periodically. Equation (9) can be obtained using $k_y = J_y \omega_n^2$.

$$\varepsilon_0 = \frac{J_z \dot{\varphi} \dot{\delta}}{J_y (\omega_n^2 - \omega^2) \sin(\omega t) + c_y \omega \cos(\omega t)} \tag{9}$$

In this paper, the energy P extracted from the damper is considered to be available for power generation, then:

$$P = \frac{c_y}{2} \omega^2 \varepsilon_0^2 = \frac{c_y}{2} \left(\frac{J_z \dot{\varphi} \omega \dot{\delta}}{J_y (\omega_n^2 - \omega^2) \sin(\omega t) + c_y \omega \cos(\omega t)} \right)^2 \tag{10}$$

It can be observed from Equation (10) that the maximum power acquisition is when the system resonates. Then, Equation (9) can be simplified as:

$$\varepsilon_0 = \frac{J_z \dot{\varphi} \dot{\delta}}{c_y \omega \cos(\omega t)} \quad (11)$$

It can be concluded from Equation (11) that ε_0 is proportional to J_z , $\dot{\varphi}$, and $\dot{\delta}$, and inversely proportional to c_y and ω , while Equation (10) can be expressed as:

$$P = \frac{c_y}{2} \omega^2 \varepsilon_0^2 = \frac{(J_z \dot{\varphi} \dot{\delta})^2}{2c_y \cos^2(\omega t)} \Rightarrow P = \frac{(J_z \dot{\varphi}) \omega \dot{\delta} \varepsilon_0}{2 \cos(\omega t)} \quad (12)$$

Equation (12) shows that for a gyroscopic device, the system output power is proportional to the flywheel angular momentum $J_z \dot{\varphi}$, the wave frequency ω , the wave pitch amplitude velocity $\dot{\delta}$, and the maximum precession angle ε_0 , on the condition that the wave has the same natural frequency as the system. It can also be considered that the output of the system power is proportional to the damping coefficient c_y of the second-order system, the square of the wave frequency ω , and the square of the maximum precession angle ε_0 . For a nonlinear system, the power expression is:

$$P = \frac{(J_z \dot{\varphi} \dot{\delta} \cos \varepsilon)^2}{2c_y \cos^2(\omega t)} = \frac{(J_z \dot{\varphi}) \omega \dot{\delta} \varepsilon_0 \cos \varepsilon}{2 \cos(\omega t)} \quad (13)$$

Compared with Equation (12), the output power in a nonlinear system is less than that in a linear system.

4. Physical Model and Test Environment

4.1. Characteristics of GWEC

As shown in Figure 3, the gyroscope wave energy converter (GWEC) system is mainly composed of a flywheel, rotor motor, support frame, speed increaser gearbox, rotating PTO, and floating platform. The flywheel rotates in one direction at high speed in the vacuum flywheel housing, and the vacuum environment bestially reduces the air resistance to the flywheel. The outer ring of the flywheel is subjected to greater centrifugal force under high-speed rotation, while the internal influence is less. Therefore, the split flywheel structure is composed of a flywheel disc and a flywheel outer ring. Among them, the flywheel disc made of titanium alloy contributes little to the moment of inertia of the flywheel. The choice of this material not only ensures strength but also reduces unnecessary weight. The high-strength and high-density X30Cr13 is adopted in the rotating mass that contributes a large moment of inertia. The rotor motor makes the load obtain a fast acceleration rate so that the system has high sensitivity and a quick response. Another advantage is that it is easy to achieve the dynamic balance of the flywheel. The small number of parts of the motor means it is simple in design and has high inherent reliability while reducing manufacturing costs. It can be seen from Figure 3 that there are circular holes arranged in a matrix on the side of the support frame. Their function is to disperse the internal stress in the frame and avoid potential safety hazards caused by stress concentration. Besides, reducing the weight of non-power output parts also can improve energy conversion efficiency. However, the precession angular velocity of the flywheel is much smaller than the rated speed of the generator. Therefore, a 4-3-3-3 gear ratio is applied to increase the precession angular velocity of the flywheel to the speed required for rotating the PTO to generate electricity. Besides, it is fixed at both ends and integrally sealed, which is not only convenient for maintenance but also highly reliable.

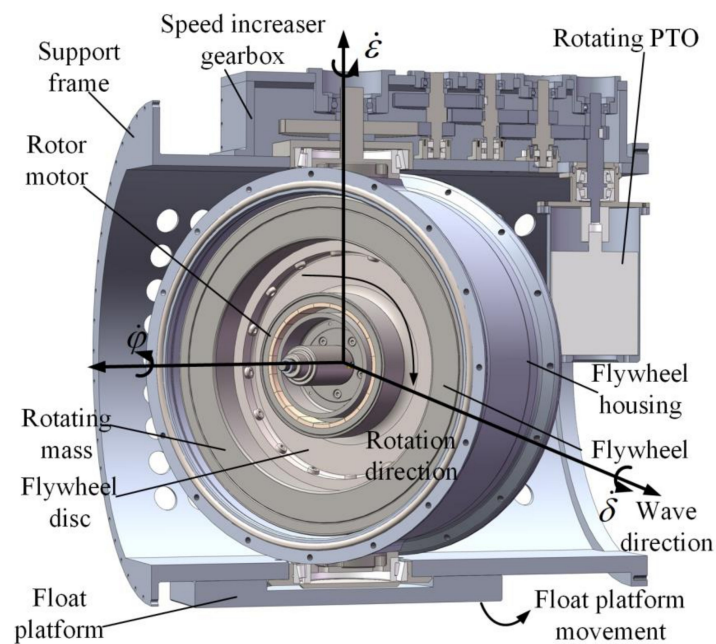


Figure 3. GWEC mechanical appearance.

Compared with other power generation devices, the GWEC converts wave energy into mechanical energy to produce electric energy directly. The device omits the intermediate transformation in the structure, thereby improving transmission efficiency. Additionally, it is sensitive to external excitation and can absorb a wider range of wave energy due to its working principle. Moreover, it is lightweight and pollution-free.

The entire device is installed in a sealed container floating on the sea surface and moored on the seabed. The movement direction of the device is strictly restricted to ensure the wave movement direction is perpendicular to the flywheel rotating direction, so that GWEC can stably convert wave energy into electric energy. Besides, a motion limit device is also added to the mechanical structure to prevent damage to the entire equipment under extreme weather conditions to improve survivability.

4.2. Test Platform and Experimental Environment

A six degrees of freedom (6-DOF) hydraulic platform is utilized to simulate the wave to test the prototype in this paper before the actual maritime experiment. This can move along three coordinate axes and rotate around three axes, and the external dimensions of the GWEC and the relative equipment of the experiment platform are shown in Figure 4.

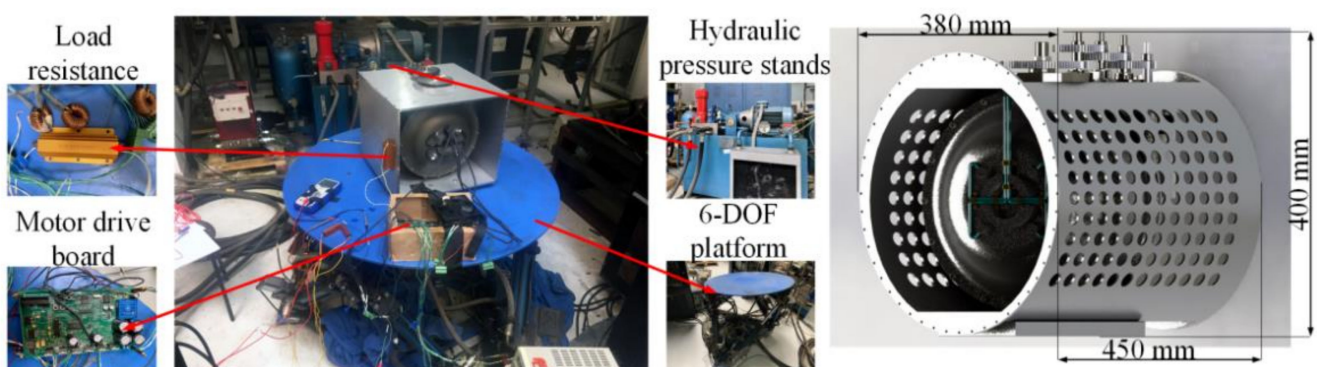


Figure 4. 6-DOF platform structure.

First, the motor drive board is powered by the power supply to drive the flywheel to rotate. Simultaneously, the 6-DOF platform is powered by the hydraulic station to simulate

wave motion and stimulate the GWEC to produce a precession effect to generate electricity. Finally, the load resistance is used to test the power output.

To facilitate installation, disassembly, and structural adjustment, a rectangular frame is used to replace the cylindrical frame in the test phase. The working space of the hydraulic 6-DOF platform is 0.4796 m³. The motor power is 7.5 kW, the system flow rate is 48 L/min, the maximum stroke of the ATOS cylinder is 280 mm with the rated pressure of 10 MPa, and each cylinder adopts the DLHZO proportional servo valve and displacement sensor. The maximum pitch range of the platform movement is $\pm 30^\circ$. The platform provides external excitation for the GWEC by simulating wave motion. The view of the GWEC with a wave simulation system and power acquisition device is illustrated in Figure 5. Among them, the 6-DOF platform controller issues instructions to make the platform simulate the movement of the regular wave during the experimental phase.

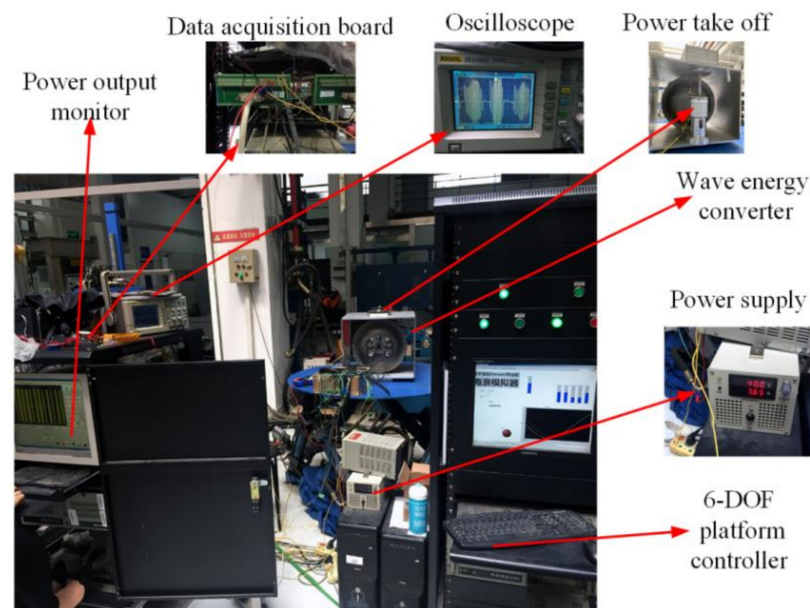


Figure 5. GWEC test system site.

The power supply is utilized to switch on the GWEC, including the operation of the gyroscope flywheel and the motor drive board. The monitor is composed of an industrial computer with A/D conversion and acquisition. The data acquisition board adopts Advantech's PCI-1716 with a 250 KS/s 16-bit A/D converter with a maximum input of 2.4 volts, which collects the voltage value of the PTO, and calculates the average power of the output through Equation (14) after filtering.

$$P = \frac{U^2}{R} \quad (14)$$

where U is the voltage value generated by the PTO after converting the gyroscope precession torque, while the load resistance R in this experiment is 100 ohms.

The drive board controls the motor to drive the flywheel to maintain a certain velocity. The speed-increasing device is used to drive the generator to generate electricity by accelerating the precession angular velocity of the flywheel. The operation of the GWEC system and power monitoring is illustrated in Figure 6. The core specification of the prototype system and rated experimental conditions are presented in Table 1.

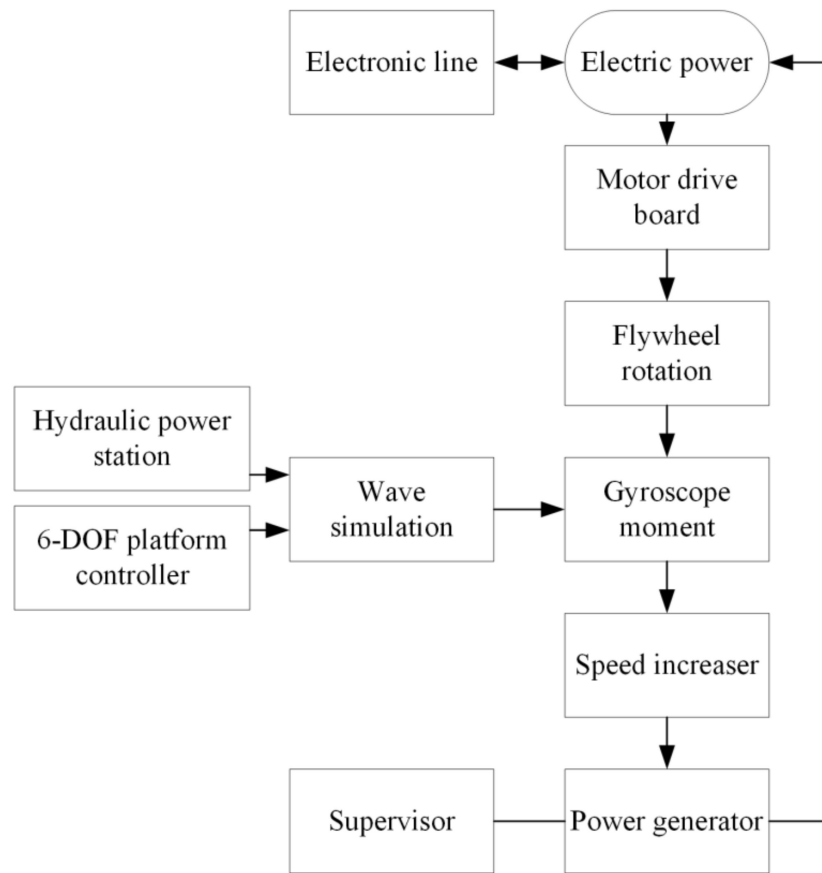


Figure 6. Operation of the gyroscope wave power generation system.

Table 1. Specification of the prototype system.

Parameter	Symbol	Values	Units
Total weight of GWEC	m_g	50	kg
GWEC volume	V	$\phi 400 \times 450$	mm^3
Weight of flywheel	m	30	kg
Moment of inertia of rotor in x axis	J_x	0.211	kgm^2
Moment of inertia of rotor in y axis	J_y	0.211	kgm^2
Moment of inertia of rotor in z axis	J_z	0.372	kgm^2
Moment of inertia of platform in x axis	J_{Px}	1.40	kgm^2
Moment of inertia of platform in y axis	J_{Py}	0.93	kgm^2
Moment of inertia of platform in z axis	J_{Pz}	1.40	kgm^2
Rated wave period	T	7	s
Rated pitch amplitude	A	10	degree ($^\circ$)
Flywheel rated speed	$\dot{\varphi}$	10,000	rpm
Damping coefficient	c_y	35	$Nm\ s/rad$
Generator rated voltage	U	24	v
Generator rated power	P	100	w

Since a 6-DOF platform is used to simulate wave motion in this experiment, the input power can be given by the total power of the platform motion:

$$P_{in} = P + \left| \frac{1}{2} J_{pz} \ddot{\delta} \right| \tag{15}$$

Due to $\delta = \delta_0 \sin(\omega t)$, and when neglecting the power to maintain the flywheel in vacuum and other energy losses, then the energy conversion efficiency is:

$$\eta = \frac{P}{P_{in}} = \frac{2J_z \dot{\varphi} \varepsilon_0}{2J_z \dot{\varphi} \varepsilon_0 + |J_{pz} \delta_0 \omega \sin(2\omega t)|} = \frac{2(J_z \dot{\varphi})^2}{2(J_z \dot{\varphi})^2 + |J_{pz} c_y \omega \sin(2\omega t)|} \quad (16)$$

From Equation (16), it is obvious that the conversion efficiency decreases as the damping coefficient c_y increases when other conditions remain unchanged. However, the damping coefficient will also change under different wave conditions and flywheel speeds. Therefore, given the strong coupling of the gyroscope system, it is impossible to directly obtain the relationship between energy conversion efficiency and other coefficients in the above formula.

5. Performance Test

To represent the performance of GWEC, the linearization model (Equation (6)) described above has a fast application, which is based on the assumption that ε is a small angle. However, the precession angle of the rotating gyroscope cannot be 0 when subjected to external forces from the mechanical and dynamic point of view. Figure 7 shows the power output of the linearized model and the nonlinearized equation under the same conditions, where the gyroscope rotating speed of Figure 7a–d is 8000 rpm and the speed in e–h is 12,000 rpm. The pitch amplitude of the left images is 6° , while that of the remaining images is 14° .

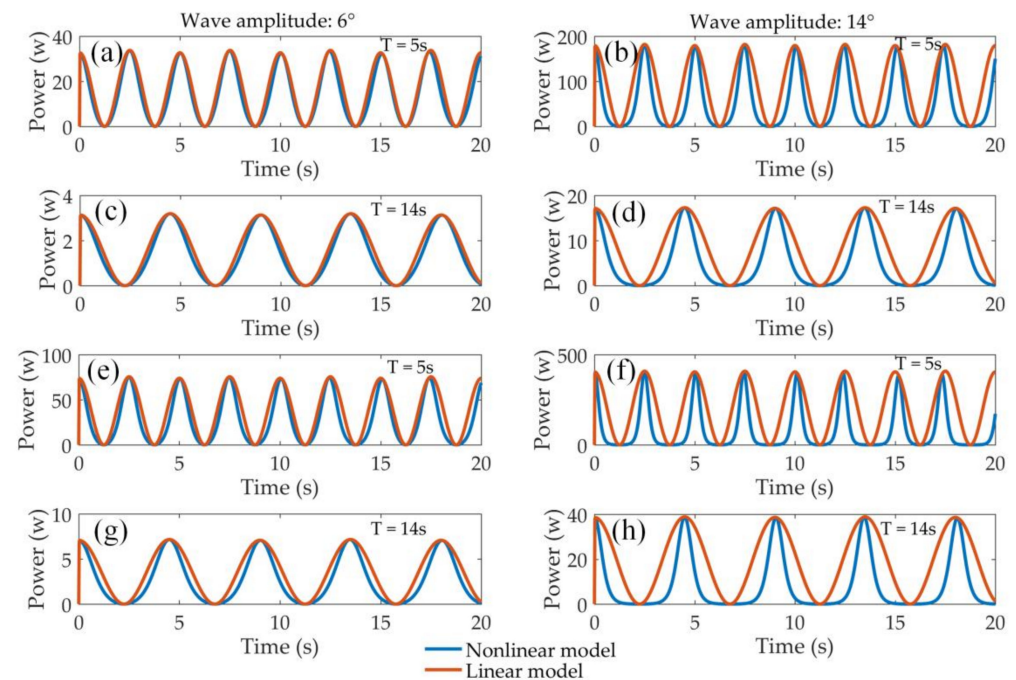


Figure 7. Comparison of power output between linear and nonlinear systems (linearized system: red line, nonlinear system: blue line): (a) $A = 6^\circ$, $T = 5$ s, $\dot{\varphi} = 8000$ rpm; (b) $A = 14^\circ$, $T = 5$ s, $\dot{\varphi} = 8000$ rpm; (c) $A = 6^\circ$, $T = 14$ s, $\dot{\varphi} = 8000$ rpm; (d) $A = 14^\circ$, $T = 14$ s, $\dot{\varphi} = 8000$ rpm; (e) $A = 6^\circ$, $T = 5$ s, $\dot{\varphi} = 12,000$ rpm; (f) $A = 14^\circ$, $T = 5$ s, $\dot{\varphi} = 12,000$ rpm; (g) $A = 6^\circ$, $T = 14$ s, $\dot{\varphi} = 12,000$ rpm; (h) $A = 14^\circ$, $T = 14$ s, $\dot{\varphi} = 12,000$ rpm.

Figure 7 shows the main differences between the linear model and the nonlinear model. In general, the power output of the linear model is greater than the nonlinear equation.

As mentioned before, Equation (5) can be simplified to Equation (6) only when ε_0 is at a small angle. When combined with Equation (12), it can be concluded that when c_y and J_z remain unchanged, the greater $\dot{\varphi}$ and A are, the greater ε_0 is. It can be clearly seen

from Figure 7 that when only the pitch amplitude is different, the output with 14° pitch amplitude A in Figure 7b,d,f,h is much greater than the others. The speed of flywheel $\dot{\varphi}$ in Figure 7e–h is also higher than in (a)–(d), which causes the increase in ε_0 . Therefore, the values of $\dot{\varphi}$ and A are both increased in Figure 7f,h, and the power difference between the linear model and the nonlinear model is more obvious than in other figures. Based on the above analysis, the following conclusions can be drawn. Under the wavelet pitch amplitude or low flywheel speeds, the linearized model can obtain an acceptable approximation of the complete nonlinear equation. However, under large pitch amplitude, or the high flywheel speed, the two models are quite different. This also verifies that the linear model can be used instead of the nonlinear model to test the characteristics of GWEC only under low-speed, small pitch amplitude conditions.

In this section, the effects of the main parameters of the gyroscope system on the output power and energy conversion efficiency are analyzed. To test and verify the performance of the GWEC, the sea state with lower wave energy density is selected in the experimental stage. The South China Sea has a wave period of 6–8 s, while the North Bay and the Gulf of Thailand have a wave height of 0.5 to 1.5 m. In this experiment, the rated sea state is set to a wave period of 7 s, and the pitch amplitude is 10° .

5.1. Effect of the Damping Coefficient

Figure 8 shows the influence of pitch amplitude on energy conversion efficiency under different damping coefficients. The energy conversion efficiency is obviously affected by the damping coefficient. As shown in Equation (16), the energy conversion efficiency generally decreases as c_y increases. The best performance is obtained with minimum damping ($c_y = 30 \text{ Nm}\cdot\text{s}/\text{rad}$) in most cases. The conversion efficiency obtained by the minimum damping coefficient is at most 1.99% higher than the efficiency corresponding to the medium damping coefficient ($c_y = 35 \text{ Nm}\cdot\text{s}/\text{rad}$). The relative maximum damping coefficient ($c_y = 40 \text{ Nm}\cdot\text{s}/\text{rad}$) is increased by at most 4.0%. It is noteworthy that not all maximum efficiency points appear at the minimum damping coefficient. As the pitch amplitude increases and the wave period decreases, the value of the damping coefficient at the point of maximum efficiency gradually increases. From a statistical point of view, the gap decreases as the pitch amplitude increases and the wave period decreases.

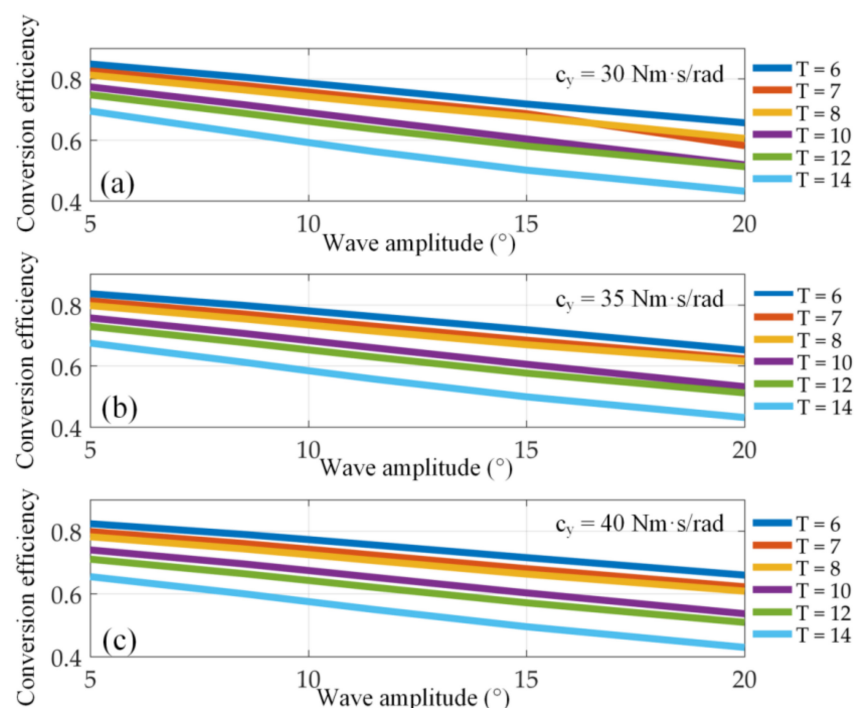


Figure 8. Influence of damping coefficient and pitch amplitude: (a) $c_y = 30$; (b) $c_y = 35$; (c) $c_y = 40$.

On the other hand, the graphs show that for a given damping coefficient and wave period, the larger the wave pitch amplitude, the lower the conversion efficiency. Besides, for the same damping coefficient and pitch amplitude, the conversion efficiency decreases with the increase in the wave period, which is especially obvious at high wave periods. In the case of small damping, the attenuation rate of the conversion efficiency with increasing pitch amplitude is greater than that with large damping. For the wave state of $T = 14$ s and $A = 5^\circ$, the conversion efficiency can be improved 4% by adjusting the damping coefficient, so an appropriate damping coefficient should be selected. This improvement is more important than changing the wave period alone (3.7% with $c_y = 40$ Nm·s/rad and $A = 20^\circ$) or the pitch amplitude alone (3.1% with $c_y = 30$ Nm·s/rad and $T = 14$ s). These results indicate that the damping coefficient should be the focus of attention when optimizing the GWEC device.

The damping coefficient is quite important due to the analysis of dynamic characteristics in Figure 9. When the damping coefficient is larger than the rated value, the output power and conversion efficiency will decrease rapidly. For damping coefficients smaller than the rated value, the precession angle will be too large, which will cause the system to be uncontrolled. The platform counter torque will decrease with the increase in the damping coefficient. From the perspective of PTO, when the damping coefficient is the optimal value, the torque on the precession shaft also reaches the maximum, which is not convenient to realize from the perspective of the mechanical structure.

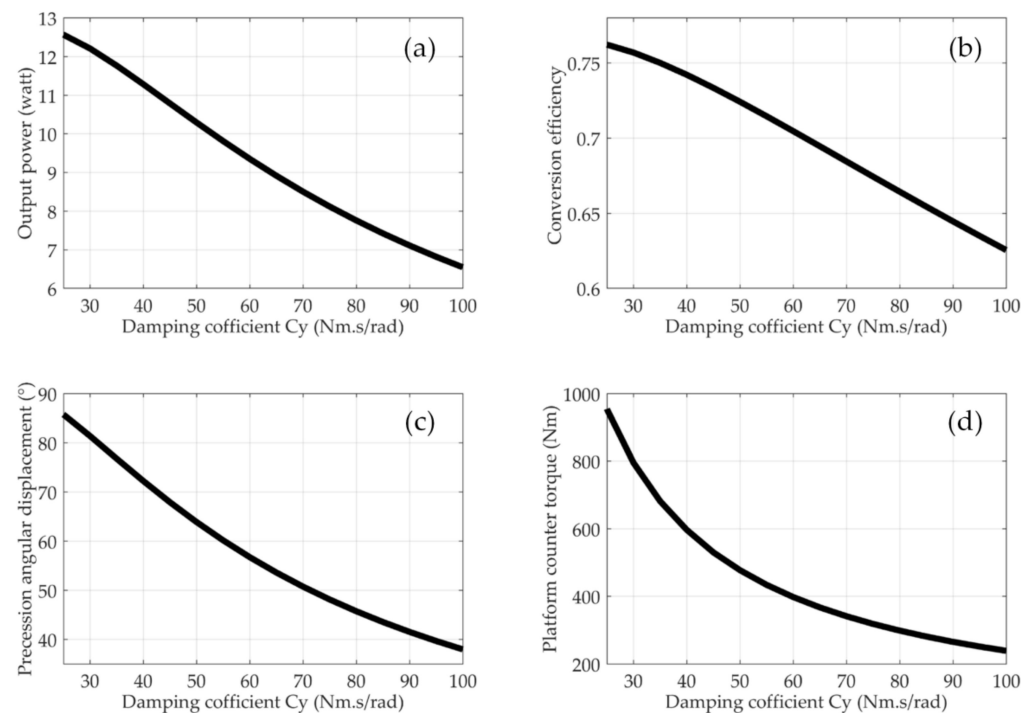


Figure 9. Effect of the PTO damping coefficient: (a) output power; (b) conversion efficiency; (c) fly-wheel precession angular displacement; (d) platform counter torque.

5.2. Effect of the Pitch Amplitude

As for the pitch amplitude of the wave in Figure 10, the output power of the system increases significantly as the pitch amplitude increases. However, the excessive amplitude will rapidly reduce the energy conversion efficiency. At the same time, this will also make the precession angular displacement reach the limit position, causing system instability. In addition, excessive platform counter torque is not conducive to energy generation.

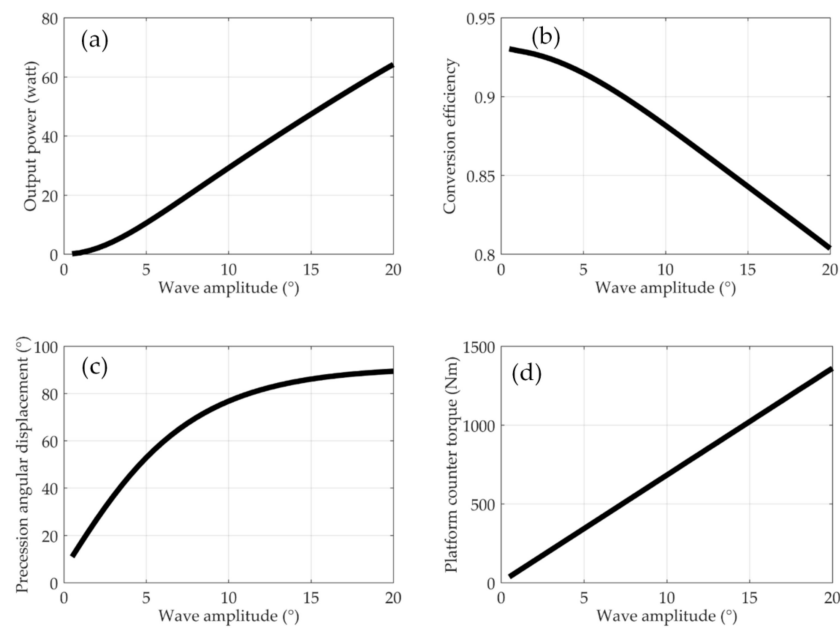


Figure 10. Effect of pitch amplitude: (a) output power; (b) conversion efficiency; (c) flywheel precession angular displacement; (d) platform counter torque.

5.3. Effect of the Flywheel Rotating Speed

Figure 11 illustrates that the flywheel rotating speed is a significant parameter in the GWEC system, and the output power increases as the flywheel rotating speed increases. When the rotating speed is less than the rated value, the conversion efficiency drops sharply, and when it is greater than the rated value, the efficiency increases slightly as the rotating speed raises. Additionally, the raising of the flywheel rotating speed will increase the precession angle displacement, while the excessive precession angle will cause the flywheel to reach the precession angle limit. The increase in the counter torque of the platform will cause the GWEC system to behave as a space stabilizer, and reduce the conversion efficiency, which is not suitable for power generation.

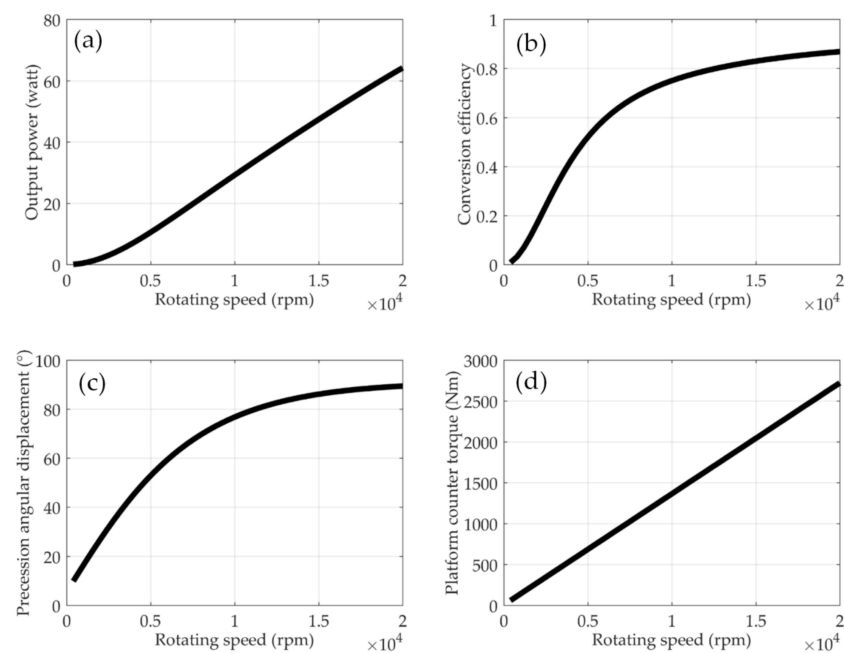


Figure 11. Effect of the flywheel rotating speed: (a) output power; (b) conversion efficiency; (c) flywheel precession angular displacement; (d) platform counter torque.

5.4. Effect of the Wave Period

Figure 12 shows the system's response to the wave period. As stated in Equation (13), the output power of the system decreases as the wave period increases. Generally, the energy conversion efficiency declines as the wave period increases. However, the changes in conversion efficiency and precession angular displacement curves were not very smooth due to the complexity of the system model. The precession angular displacement decreases rapidly with the wave period from 5 to 12 s, and the trend reduces gently after 12 s. The counter torque of the platform decreases as the wave period increases.

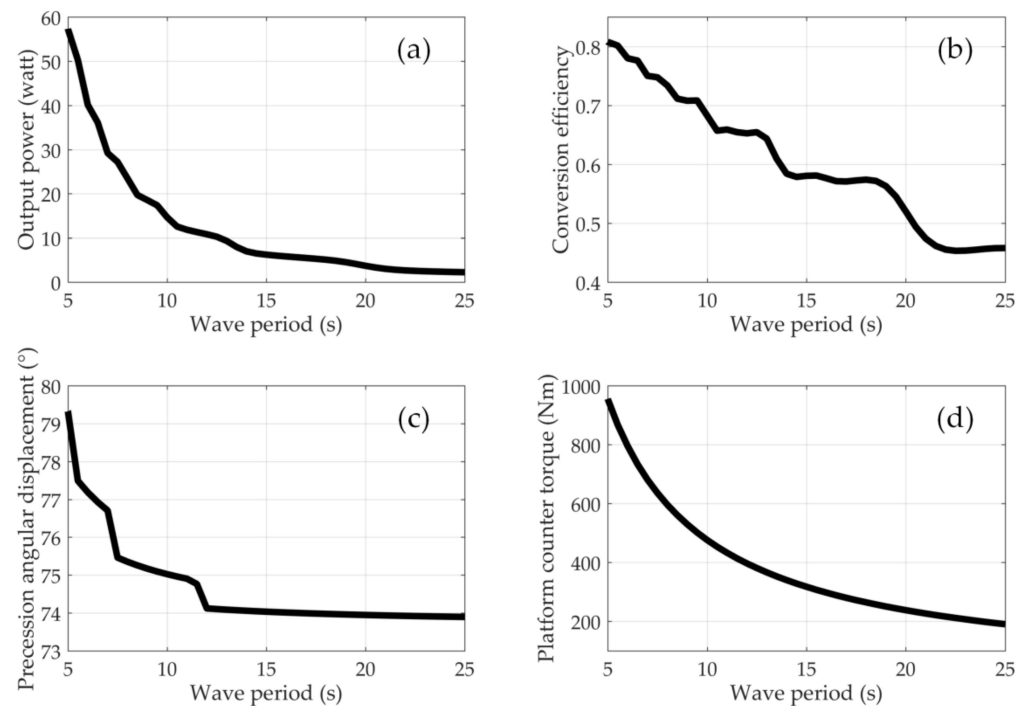


Figure 12. Effect of the wave period: (a) output power; (b) conversion efficiency; (c) flywheel precession angular displacement; (d) platform counter torque.

As mentioned earlier, the energy conversion efficiency varies with the wave period. To maximize energy conversion efficiency, Figure 13 shows the efficiency relative to the wave period and flywheel rotating speed. The efficiency increases as the wave period decreases and the speed of the flywheel increases. However, if the period is short, the conversion efficiency decreases significantly at low speed, but it can be increased in phases by raising the flywheel rotating speed. For high speed, reducing the wave period does not improve efficiency significantly in the simulation situation. As for the actual system, the trade-off between energy output and power consumption when maintaining the high-speed rotation of the flywheel is also considered to determine the optimal flywheel rotating speed in various situations.

5.5. Multiple Regression and Prediction

Figure 14 shows the effect of changes in damping coefficient, pitch amplitude, wave period, and flywheel speed on output power. In order to observe the influence of the changes of the two parameters on the output power of the system, we kept the other two parameters at the rated values in each figure. The theoretical output power will increase with the decrease in the wave period, the raising of the pitch amplitude, and the increase in the flywheel speed, no matter how the parameters change. More importantly, an appropriate damping coefficient needs to be selected. In the case of $A = 10^\circ$ and $\dot{\varphi} = 10,000$ rpm, the maximum power of 46.06 W was achieved at $T = 5$ s and $c_y = 30$ Nm·s/rad rather than $c_y = 25$ or 35 Nm·s/rad, in Figure 14a. Figure 14b–d shows that the power changes slowly

with the parameters, but in Figure 14e,f, it can be observed that the output increases sharply when the wave period is less than 6 s. It is also worth noting that comparing Figure 14c–f, the influence of pitch amplitude and flywheel speed on output power is almost the same.

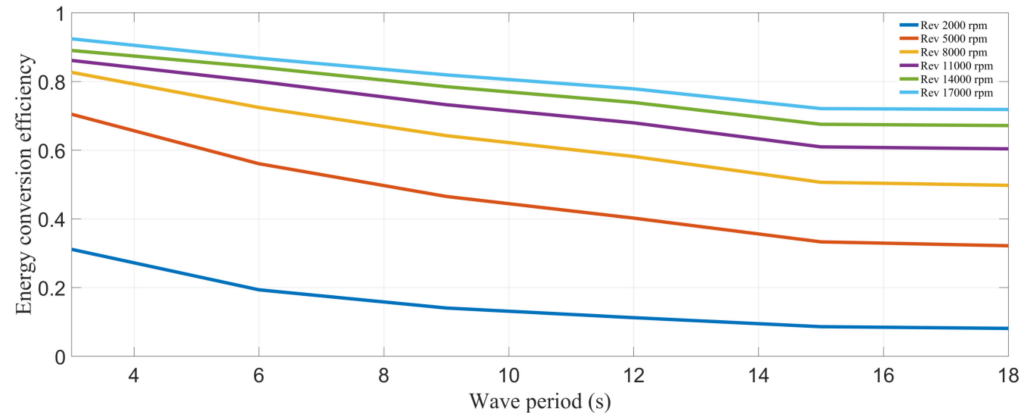


Figure 13. The influence of wave period.

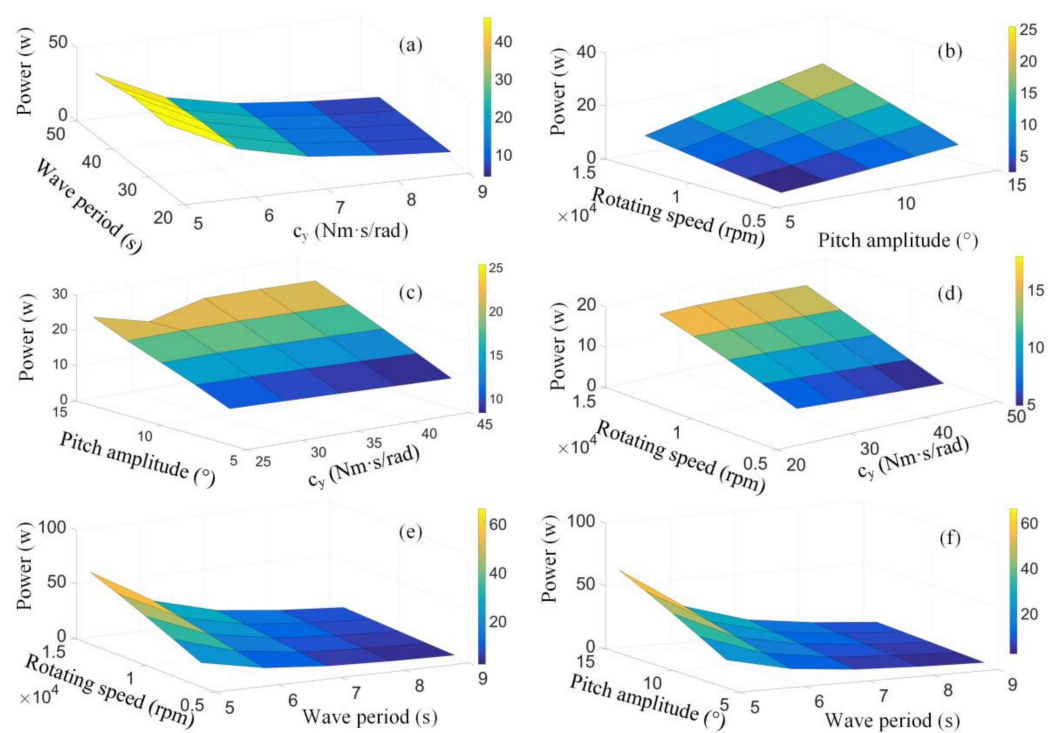


Figure 14. The influence of input parameters on power output: (a) P vs. c_y , T; (b) P vs. A, ϕ ; (c) P vs. c_y , A; (d) P vs. c_y , ϕ ; (e) P vs. T, ϕ ; (f) P vs. T, A.

Minitab was used to perform multiple linear regression and power prediction on the previous data in Figure 15. The figure shows the damping coefficient X1 ($c_y = 30, 35, 40$ Nm s/rad), the flywheel rotating speed X2 (Rev = 9000, 10,000, 11,000 rpm), the wave period X3 ($T = 6, 7, 8$ s), and the wave pitch amplitude X4 ($A = 9^\circ, 10^\circ, 11^\circ$) to obtain the statistical results of output power simulation.

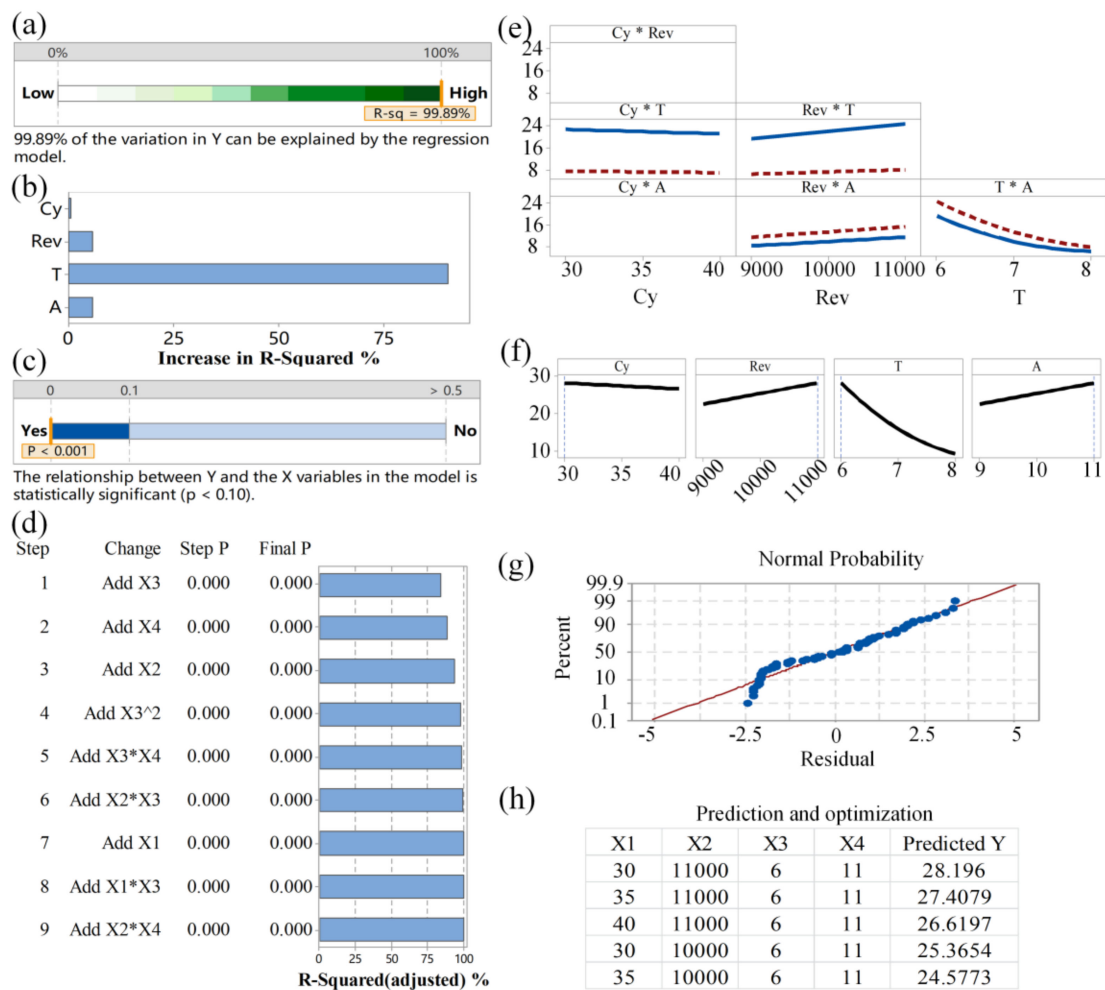


Figure 15. Multiple regression analysis and power prediction: (a) R-sq report; (b) contribution of each parameter in R-sq; (c) P value; (d) R-sq (adj) report; (e) parameter interactive analysis; (f) influence of parameters on output; (g) residual analysis; (h) prediction and optimization report.

The complete output formula of power is expressed in Figure 15a. Power = $70.15 - 0.4581 \times 1 + 0.006638X_2 - 30.493X_3 + 6.639X_4 + 2.8507X_3^2 + 0.05007X_1 \times X_3 - 0.000925X_2 \times X_3 + 0.000158X_2 \times X_4 - 0.9250X_3 \times X_4$. R-sq is a measure of fit, which is defined as the ratio of regression model error to total error. The R-sq value of the model is 99.89% in Figure 15a, which indicates an excellent correlation between the experimental value and the fitted value. T contributed the most to the model, while C_y contributed the least in Figure 15b. A low p -value ($p \leq 0.1$) implies that the relevant data source is statistically significant. The P-value is less than 0.001 in this regression, which also indicates the obtained model is considered statistically significant and desirable in Figure 15c. Differently from R-sq, when the added variables in the model are not statistically significant, R-sq (adj) will decrease, so R-sq (adj) is one of the important indicators to measure the quality of the model built. The larger the R-sq (adj), the better the model fits. Among the variables, the R-sq (adj) of the minimum value X_3 is greater than 80%, indicating the system has high goodness of fit in Figure 15d.

Figure 15e,f shows the interaction of the variables and the effect of every single variable on the output. Intersecting lines are used to indicate significant interactions; however, there are no two important interactions in Figure 15e. There is even no mutual influence between C_y and Rev or A. Among the individual effects of the four variables on the output, T has the largest impact on the power in Figure 15f, while other variables have less impact on the output in a small range of changes, which is the same as the simulation conclusion.

Residual plots for power are shown in Figure 15g. The residual is the difference between the actual observation value and that fitted from the regression. When the points on the plot fall near the straight line, it indicates the data are normally distributed. It can be clearly seen from the figure that the experimental points are all near the straight line, which verifies the data are normally distributed. By comparing 81 sets of simulation results with multiple linear regression data, we get an average power error of 0.0375, and a variance of 0.0245, which also verifies the effectiveness of the model.

The prediction and optimization report in Figure 15h provides an ideal output scheme for pursuing maximum power goals. The predicted result according to the model is 28.196 W, which is 99.37% compared to the simulated value of 28.375 W. This proves the model has excellent fitting and predictive capabilities, and the linear regression formula in the modeling report can be applied to accurately predict power output. Besides, the other top four alternative solutions with predicted power closest to the optimal solution are presented.

6. The Proposed Modified P&O

6.1. Adaptive Perturbation Size

From Figures 8–13, it can be concluded that the energy output under a single variable has a single peak, and there is a unique optimal output power in every sea state. Moreover, it can be concluded from Figures 14 and 15 that under the combined action of the two input conditions, the power output has the only optimal damping coefficient. However, this parameter is also variable under different sea conditions and flywheel rotating speeds. At present, the MPPT algorithm has been widely used in energy fields, and the principle is applied to electronic PWM control to optimize the generator load. The P&O control algorithm is widely used in MPPT of photovoltaic power generation, which is simple and has excellent convergence. Its working principle is to adjust the perturbation direction according to the comparison result of the power value before and after the perturbation signal.

$$X_{new} = X_{old} + \Delta X \times \phi \quad (17)$$

In Equation (17), X is the control variable, which can be voltage (U), current (I), or duty cycle (d), and ΔX is the perturbation step size. Simultaneously, ϕ represents the direction of perturbation, and $+1$ and -1 correspond to the increase and decrease in X . However, the working point cannot be stabilized at the MPP, and will fluctuate around the stable power as the perturbation changes. Therefore, it is necessary to obtain an adaptive perturbation step size Δx to ensure the power loss when fluctuation around the MPP is minimized.

The inverse proportional function is a common mathematical function, the expression of which is $y = k/x$. The conventional inverse proportional function makes the product of two consecutive perturbation steps a fixed value, which not only has strict requirements on the value of the constant but also inevitably produces energy waste caused by oscillation. A dynamic inverse proportional function method to adjust the size of the perturbation step is applied in this paper. Define that the product of two consecutive perturbation steps is equal to the absolute value of ΔP : $|\Delta p| = step_{n-1} \cdot step_n$.

After assigning an initial step size a , this formula ensures the perturbation step size will vary with the change of ΔP . Besides, no matter how the external conditions change, ΔP and the perturbation size will not be zero to ensure the stability of the algorithm. After the initial perturbation step length is given, when the value of ΔP is larger, the perturbation size will increase accordingly, thereby reducing ΔP . At this time, the new perturbation step size will decrease with the decrease in ΔP , and the power output will reach the vicinity of MPP eventually.

6.2. Minimize Steady-State Error

It can be concluded from Equation (17) that the perturbation step size is closely related to the value of ϕ . In this paper, five consecutive ϕ are recorded to detect oscillations, and extra step size is applied to reduce steady-state power loss. When the power is increased

or decreased, the absolute value of five consecutive ϕ is 5, and when the steady-state oscillation occurs, the sum of the absolute values is less than 5 as is shown in Equation (17). Therefore, it can be accurately detected whether it reaches the vicinity of MPP by recording five consecutive ϕ .

$$if \left| \int_1^5 \phi \right| = \begin{cases} 5 \dots \dots \text{(Non-steady state)} \\ else \dots \dots \text{(Steady state)} \end{cases} \quad (18)$$

Equation (18) can be applied as a criterion to switch the perturbation step size. The perturbation step size is calculated by the inverse proportional function when the system is in an unstable state. When $\left| \int_1^5 \phi \right| = 3$, it indicates that the operating point has reached the vicinity of MPP, so a small step size is used to reduce the oscillation. Even when the system is in steady-state, especially when $\left| \int_1^5 \phi \right|$ is 1, and the operating point is closer to the MPP, an extra small perturbation step size is applied. In this way, not only can the perturbation step size be switched in different states of the system to ensure rapidity, but the application of the extra step size when the system is near the MPP can greatly reduce the power loss in the steady state.

6.3. Algorithm Flowchart

The modified algorithm is illustrated in the flowchart of Figure 16. The first step is to initialize each parameter and assign variables. In this paper, the limited range is imposed on the constant of the inverse proportional function to ensure the change of the step size twice in succession. In this case, a large step size can be used when the power difference is large to ensure the rapidity of the system, and small step size can be applied when it reaches the vicinity of the MPP to reduce energy loss. It is worth noting that since the precise MPP position will continue to move, zero perturbation is not allowed, which will force the tracking of the same voltage value throughout the cycle, resulting in a serious reduction in efficiency.

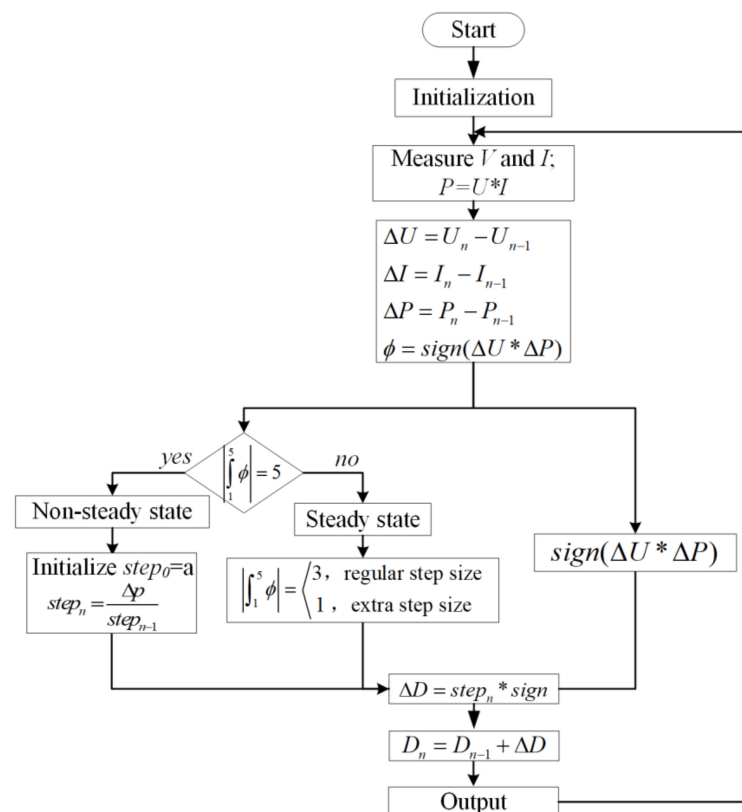


Figure 16. The complete flowchart of the modified P&O.

The overall simulation flow chart in MATLAB/Simulink is shown in Figure 17. The pitch amplitude and period are the input parameters of the wave, and the angular displacement and angular velocity of precession are applied to the inputs of the PTO. The duty cycle is generated by the MPPT algorithm and applied to the boost chopper. Finally, the smooth power curve is obtained by the filter module.

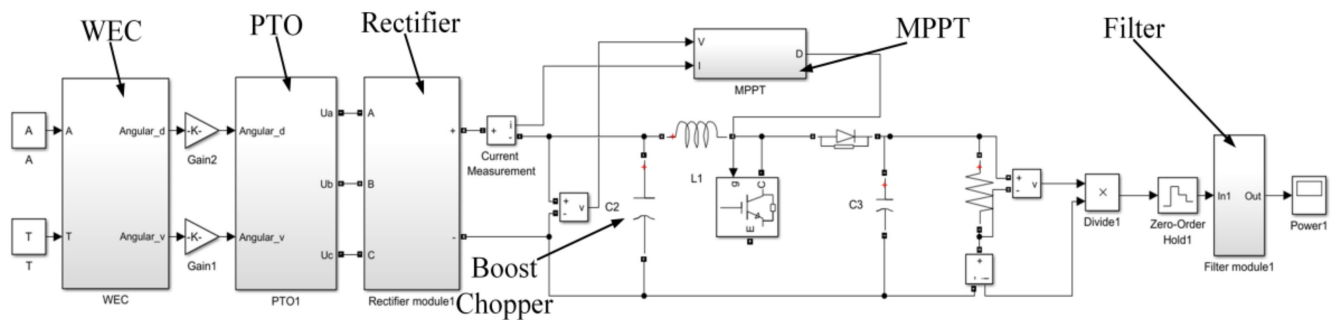


Figure 17. The diagram of simulation in Simulink, including WEC, PTO, rectification, filtering, and MPPT algorithm by MATLAB.

7. Algorithm Simulation and Experimental Verification

7.1. Filter Comparison

Compared with relatively stable solar energy, wave energy changes continuously, and its energy output fluctuates greatly. The application of filters is very necessary to obtain a smooth and stable output power curve and reduce unnecessary interference. Butterworth and Chebyshev Type II filters are universal and very effective low-pass filters in signal processing, which can eliminate overshoot in the system. However, the system will have some oscillation, if rapidity is the primary goal. For signal processing, the lower the cut-off frequency of the filter and the longer the equivalent time delay, the slower the sensor response speed, which will cause phase lag. Therefore, a lead circuit needs to be added to the circuit to compensate for the phase lag, which will increase the amount of calculation and complicate the system structure. As a linear filtering method, mean filtering is usually applied in image processing, which has the advantages of high efficiency, simple structure, and less calculation. It can not only effectively filter random interference signals, but also smooth the output curve.

The power output comparison of different filtering methods under rated conditions is shown in Figure 18. In the waveform diagram after the initial filtering, the waveform without subsequent filtering has the worst performance and the most intense oscillation. However, Butterworth and Chebyshev Type II filters perform equally, and both are better than unfiltered. Their steady-state error is slightly larger when the two provide better rapidity. The average filter with a step size of $5e-1$ has the smallest steady-state error. The stability criterion of the system is fully demonstrated in this method, but the rapidity of this method is too poor to meet the system requirements. Compared with other methods, the average filter with a size of $1e-1$ guarantees the excellent stability and good rapidity, especially after reaching the rated operating point, and the energy oscillation is much smaller than the other two filtering methods. The average power generation in 25 s obtained by the MPPT control is 10.9 W, which accounts for 85.96% of the optimal power generation obtained by data fitting, which directly proves the feasibility of the algorithm.

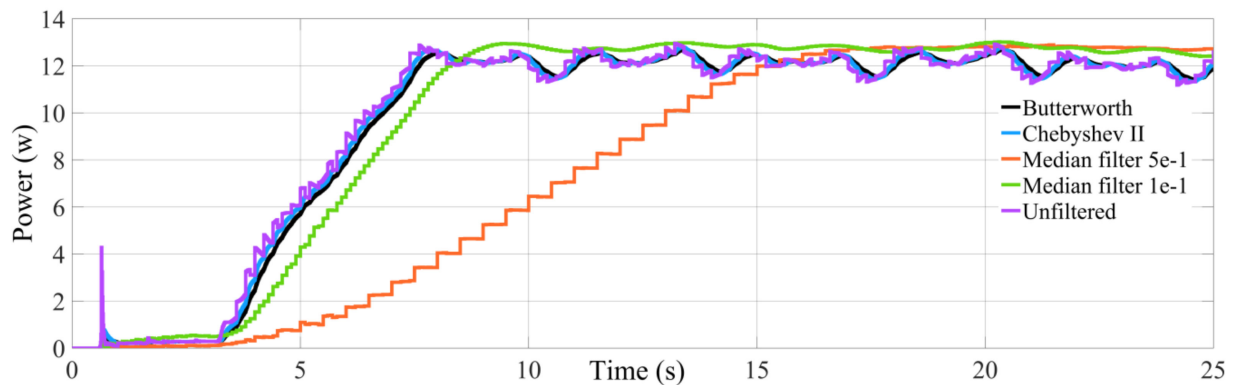


Figure 18. Power output comparison of different filtering methods under rated conditions.

7.2. Simulation of Different Sea Conditions

The motion state of the waves will change with the water depth. Waves in shallow waters will undergo refraction, reflections, and other phenomena due to the impact of coastal terrain and offshore engineering, which can be regarded as a superposition of regular waves. In deep-water areas, the wave period usually fluctuates very little within a few hours. Therefore, the deep-water waves with a narrow spectrum can be regarded as regular waves with relatively excellent predictability, except for occasional amplitude changes. In this section, we analyze the performance of the modified algorithm under different ocean conditions.

The simulation model was established by MATLAB/Simulink according to the design to verify the proposed control algorithm. First, under the rated conditions, the wave period is set to 7 s, the pitch amplitude is 10° , and the simulation time is 25 s. A traditional P&O algorithm with a fixed step size of $1e-1$ and $1e-2$ is established to facilitate comparison. The comparison between the outputs and the modified MPPT is shown in Figure 19.

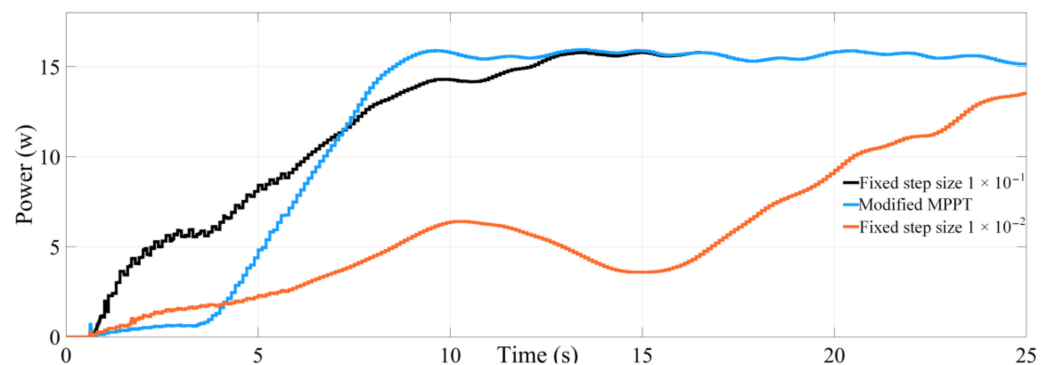


Figure 19. Power comparison chart.

As mentioned earlier, the choice of step size is particularly important. It can be clearly seen from Figure 19 that the fixed step method has certain disadvantages. When the step size is slightly larger (step size = 1×10^{-1}), the tracking curve has good rapidity, especially in the initial position. However, there are large power fluctuations in the initial stage of the simulation, which has a great impact on the PTO and is not conducive to stable energy generation. Moreover, there will be a short-term constant output phenomenon at non-MPP (2.5–3.5s), which has a certain impact on the rapidity of the algorithm. As for the small step size (step size = 1×10^{-2}), the tracking characteristics are extremely poor, and the MPP cannot be reached before the end of the entire simulation cycle. This dynamic characteristic is not satisfactory. The modified MPPT method has both good speed and excellent stability under rated conditions.

Some scenarios of varying wave pitch amplitude were simulated to test the control strategy of this article, and the ocean state (the MPP of the system) changes. Among them, Figure 20a,b has increased and decreased step signals at 12.5 s, respectively. In Figure 20c,d, the ramp increase and decrease signals last from 10 to 15 s, respectively. In Figure 20e,f, there are half-sine signals that increase and decrease from 10 to 15 s. It can be seen from Figure 20 that the system starts running from 0 and operates stably around the rated MPP from 8 s, which shows that the filter module effectively solves the system oscillation problem near the MPP. At 10–15 s, the pitch amplitude changes differently. However, after a period of time, the system can accurately find a new MPP and operate stably no matter how the wave energy changes.

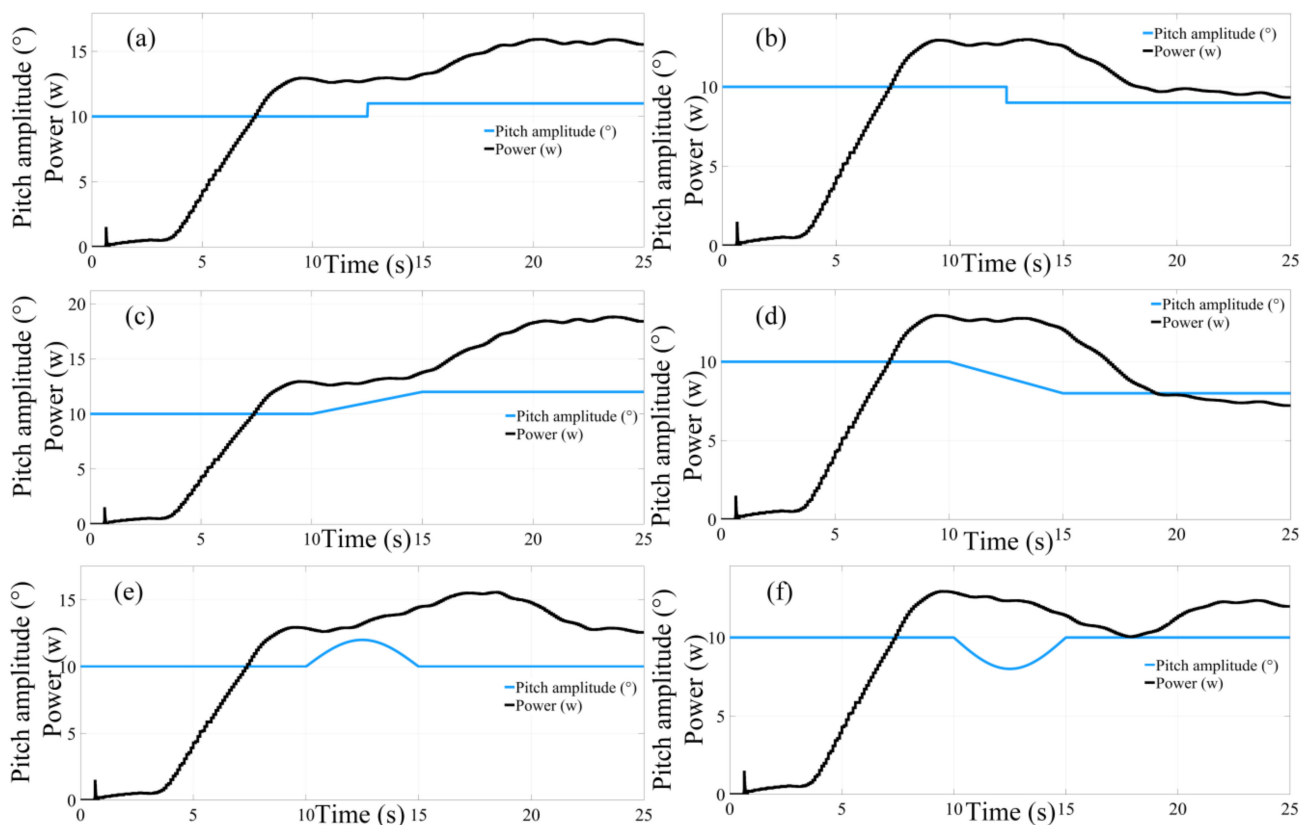


Figure 20. Power output curve under different ocean conditions: (a) step signal 10° – 11° ; (b) step signal 11° – 10° ; (c) ramp signal 10° – 12° ; (d) ramp signal 10° – 8° ; (e) half-sine signal 10° – 12° – 10° ; (f) half-sine signal 10° – 8° – 10° .

In order to test the performance of the MPPT proposed in this paper, two modified algorithms are added to the comparison; one comes from [9], and algorithm 2 comes from [10]. Figure 21 shows the power output comparison of different methods under rated sea conditions.

Figure 21a shows the angular displacement and angular velocity of the flywheel output under rated sea conditions, both of which change smoothly and have the same period. Figure 21b shows the power output of different methods under this sea state. The initial step of algorithm 1 is large, which presents an excellent dynamic response. However, in the process of chasing MPP, a strong oscillation is not conducive to energy output. The proposed algorithm has both rapidity and smooth power output, which avoids system oscillation. The initial step size of algorithm 2 is small, and it takes the longest time to reach the position of MPP, but the output curve of this method is relatively stable. The above three methods have reached MPP, verifying the feasibility of the methods.

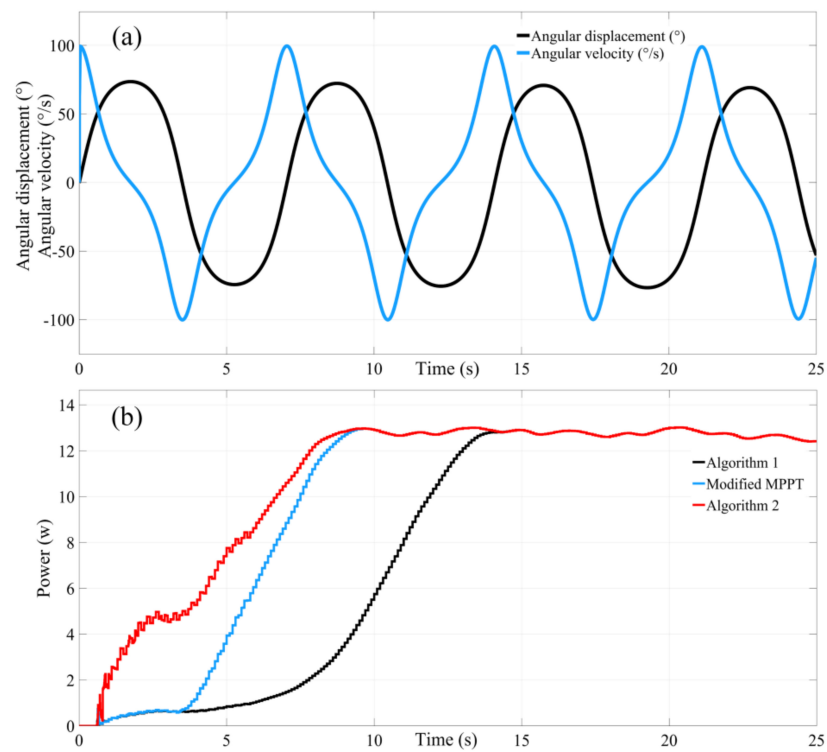


Figure 21. Algorithm comparison of rated sea conditions: (a) precession angular displacement and angular velocity under rated conditions; (b) power output of three methods.

However, in the shallow areas of the ocean, especially the coastal areas, the wave conditions are more complicated. Therefore, this paper superimposes random waves in the rated sea state to simulate the actual sea area, in order to verify the performance of the algorithm in the coastal sea area. The power output comparison is shown in Figure 22.

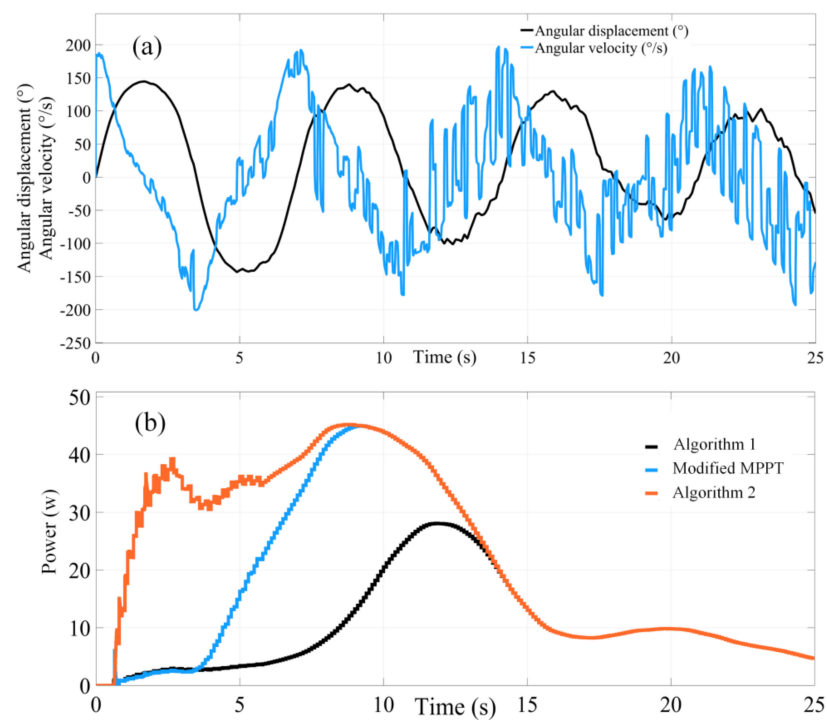


Figure 22. Algorithm comparison of time-varying sea conditions: (a) precession angular displacement and angular velocity under irregular sea conditions; (b) power output of three methods.

Figure 22a shows the flywheel output angular displacement and angular velocity under irregular sea conditions. It can be clearly seen from the figure that the overall trend of precession angular displacement is sinusoidal, accompanied by continuous oscillation, and the change of its amplitude decreases with time. The precession angular velocity curve contains continuous and strong fluctuations, and it is difficult to find the law of motion. In this wave state, three different MPPT methods are shown in Figure 22b. In general, the performance of the three algorithms is the same as that shown in Figure 21b. Algorithm 1 is very fast, but it is full of strong power oscillations in the process of chasing MPP. The algorithm proposed in this paper is known for its stable output power and certain rapidity. However, algorithm 2 exposes the problem of poor dynamic response and poor power tracking in the initial stage. Eventually, the three algorithms reached MPP at 14 s simultaneously, and followed MPP steadily as the wave conditions changed.

7.3. Experimental Test

Figure 23 illustrates the actual influences of different flywheel rotating speeds, wave periods, and pitch amplitude on output power. Under the same conditions, the output power improves as the wave period decreases, the flywheel rotating speed raises, and the pitch amplitude increases, which also verifies the previous simulation. From Figure 23a,b, it can be concluded that the modified MPPT control algorithm takes approximately 10 s to reach the vicinity of MPP and maintain a stable output. This also proves the feasibility and stability of the algorithm under different working conditions. It can be observed from the figure that the peak voltage of the power output is approximately 50 V, and the output period is the same as the wave. It is worth noting that there is still a certain gap between the output power and the theoretical power in each experimental state in the figure. The experimental power of Figure 23d is 13.8 W, which is only 0.92 W lower than the theoretical output, accounting for 93.8% of the maximum power. However, the actual output of Figure 23a is 6.1 W, which is 1.15 W smaller than the simulated value, and only reaches 84.2% of the simulated maximum power, which is the smallest proportion in Figure 23. The ratio of the actual power to the theoretical power value in Figure 23b is 91.1%, and the ratio in Figure 23c is 85.0%. The power difference between theory and reality is affected by factors such as the mechanical efficiency of the transmission mechanism, friction, and electrical losses. After comparing all the actual outputs and the simulated values, it can be concluded that the difference between the two values is almost the same under different working conditions.

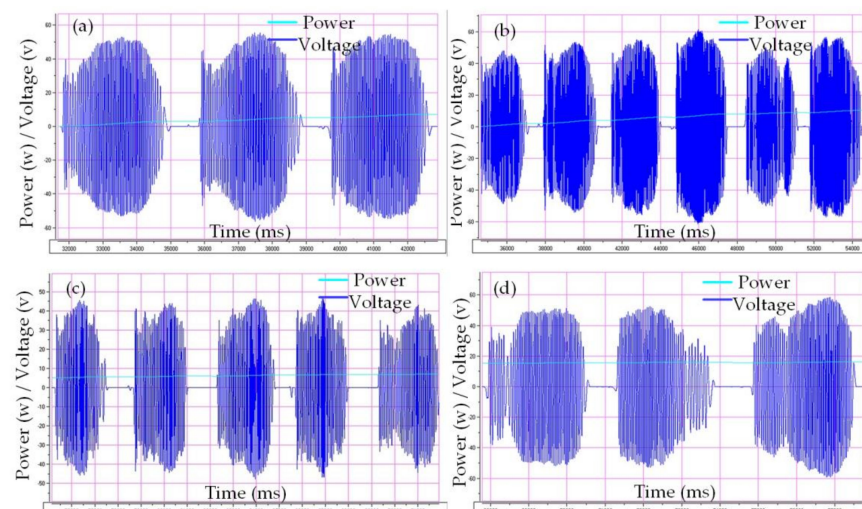


Figure 23. Effect of different input parameters on output power (the dark line is the voltage measurement value, the light line is the MPPT output): (a) $\dot{\varphi} = 10,000$ rpm, $T = 8$ s, $A = 10^\circ$, $P = 6.1$ W; (b) $\dot{\varphi} = 10,000$ rpm, $T = 7$ s, $A = 10^\circ$, $P = 10.7$ W; (c) $\dot{\varphi} = 8000$ rpm, $T = 7$ s, $A = 10^\circ$, $P = 7.4$ W; (d) $\dot{\varphi} = 10,000$ rpm, $T = 7$ s, $A = 12^\circ$, $P = 13.8$ W.

8. Conclusions

This paper proposes a modified MPPT algorithm and realizes the maximum power capture under different working conditions based on the gyroscope WEC. The main work of this paper is as follows:

1. The paper introduces the working principle of the gyroscope wave energy converter, and the energy conversion process. The influence of the natural frequency, damping ratio, and input parameters of the wave condition on the power output are analyzed. The complete expression of the power output under wave energy is obtained;

2. We conclude from the dynamic model of the system that the linear model can be used to replace the nonlinear model when the precession angle is small. The influence of each input parameter on power, conversion efficiency, and the experimental platform is analyzed, and the single-peak function of power output is verified. The linear equation of the output power is obtained through multiple linear regression, and the correctness of the regression analysis is verified by the prediction model;

3. This paper proposes a modified MPPT algorithm based on the traditional P&O method which focuses on improving the stability of power output and ensuring certain dynamic characteristics. The basic idea of the algorithm is to dynamically adjust the perturbation step length with an inverse proportional function to ensure the stability of the system while achieving rapidity. The sign of the power difference is used to determine whether the system is in a steady state, and smaller step size is applied to reduce the steady-state error. The adopted mean filtering function provides the system with strong robustness and an excellent ability to adapt to changes in external conditions;

4. The proposed algorithm is compared with the fixed size algorithm under the rated condition. The simulation results show that the method has a faster dynamic response, better stability, and smoother output power curve. Then, two variable step size algorithms are introduced to compare with the proposed algorithm under different sea states. The results illustrate that the proposed algorithm has excellent stability and rapidity. Eventually, experimental results verify that the designed MPPT control algorithm can effectively maximize power generation under different conditions.

9. Future Work

Future work includes establishing a hydrodynamic model of the device, optimizing the overall dimensions and mass distribution of the floating body, and establishing a detailed mooring system. It also includes reducing system power loss, and matching the appropriate flywheel speed according to the motor power consumption. More intelligent algorithms to achieve optimal or sub-optimal control will be developed to improve power performance under different conditions. We will verify the performance of the proposed algorithm and control strategy in the wave tank or the ocean to obtain experimental feedback on the results on the simulation and test platform. We could develop commercial applications of equipment, such as the electric source of the buoy for signal light, or form a variety of distributed power applications to power small islands or ports.

Author Contributions: Conceptualization, H.J. and Z.P.; methodology, H.J.; software, H.J.; validation, Z.P. and Z.T.; investigation, Z.T.; resources, Z.P.; data curation, Z.T.; writing—original draft preparation, H.J.; writing—review and editing, H.J.; visualization, Z.T.; supervision, Z.P. All authors have read and agreed to the published version of the manuscript.

Funding: This research received no external funding.

Institutional Review Board Statement: Not applicable.

Informed Consent Statement: Not applicable.

Data Availability Statement: No new data was created or analyzed in this study. Data sharing does not apply to this article.

Conflicts of Interest: The authors declare no conflict of interest.

References

1. Derbeli, M.; Barambones, O.; Sbita, L. A Robust Maximum Power Point Tracking Control Method for a PEM Fuel Cell Power System. *Appl. Sci.* **2018**, *8*, 2449. [[CrossRef](#)]
2. Chen, M.; Ma, S.; Wu, J.; Huang, L. Analysis of MPPT Failure and Development of an Augmented Nonlinear Controller for MPPT of Photovoltaic Systems under Partial Shading Conditions. *Appl. Sci.* **2017**, *7*, 95. [[CrossRef](#)]
3. Falnes, J.; Perlin, M. Perlin, Ocean Waves and Oscillating Systems: Linear Interactions Including Wave-Energy Extraction. *Appl. Mech. Rev.* **2003**, *56*, B3. [[CrossRef](#)]
4. Bracco, G.; Giorcelli, E.; Mattiazzo, G. ISWEC: A gyroscopic mechanism for wave power exploitation. *Mech. Mach. Theory* **2011**, *46*, 1411–1424. [[CrossRef](#)]
5. Choi, Y.D.; Kim, C.G.; Kim, Y.T.; Song, J.I.; Lee, Y.H. A performance study on a direct drive hydro turbine for wave energy converter. *J. Mech. Sci. Technol.* **2010**, *24*, 2197–2206. [[CrossRef](#)]
6. Tongphong, W.; Kim, B.H.; Kim, I.C.; Lee, Y.H. A study on the design and performance of ModuleRaft wave energy converter. *Renew. Energy* **2021**, *163*, 649–673. [[CrossRef](#)]
7. Hughes, M.G.; Heap, A.D. Heap, National-scale wave energy resource assessment for Australia. *Renew. Energy* **2010**, *35*, 1783–1791. [[CrossRef](#)]
8. Neshat, M.; Sergiienko, N.Y.; Amini, E.; Nezhad, M.M.; Garcia, D.A.; Alexander, B.; Wagner, M. A New Bi-Level Optimisation Framework for Optimising a Multi-Mode Wave Energy Converter Design: A Case Study for the Marettimo Island, Mediterranean Sea. *Energies* **2020**, *13*, 5498. [[CrossRef](#)]
9. Sorensen, H.; Friis-Madsen, E.; Christensen, L.; Kofoed, J.P.; Frigaard, P.B.; Knapp, W. The Results of Two Years Testing in Real Sea of Wave Dragon. In Proceedings of the 6th European Wave and Tidal Energy Conference: EWTEC 2005, Glasgow, UK, 29 August–2 September 2005.
10. Evans, D.V.; Antonio, F.D.O. *Hydrodynamics of Ocean Wave-Energy Utilization*; Springer: Berlin/Heidelberg, Germany, 1985.
11. Falcão, A.D.O.; Justino, P.A.P. OWC wave energy devices with air flow control. *Ocean Eng.* **1999**, *26*, 1275–1295. [[CrossRef](#)]
12. Todalshaug, J.H.; Ásgeirsson, G.S.; Hjálmarsson, E.; Mailliet, J.; Möller, P.; Pires, P.; Guérinel, M.; Lopes, M. Tank testing of an inherently phase-controlled wave energy converter. *Int. J. Mar. Energy* **2016**, *15*, 68–84. [[CrossRef](#)]
13. Beatty, S.J.; Hall, M.; Buckham, B.J.; Wild, P.; Bocking, B. Experimental and numerical comparisons of self-reacting point absorber wave energy converters in regular waves. *Ocean Eng.* **2015**, *104*, 370–386. [[CrossRef](#)]
14. Falcão, A.F.O.; Henriques, J.C. Oscillating-water-column wave energy converters and air turbines: A review. *Renew. Energy* **2016**, *85*, 1391–1424. [[CrossRef](#)]
15. Giorgi, G.; Ringwood, J. Parametric motion detection for an oscillating water column spar buoy. In *Advances in Renewable Energies Offshore*; Taylor & Francis: London, UK, 2018; pp. 502–512.
16. Renzi, E.; Doherty, K.; Henry, A.; Dias, F. How does Oyster work? The simple interpretation of Oyster mathematics. *Eur. J. Mech. B Fluids* **2014**, *47*, 124–131. [[CrossRef](#)]
17. Murakami, T.; Imai, Y.; Nagata, S. Experimental study on load characteristics in a floating type pendulum wave energy converter. *J. Therm. Sci.* **2014**, *23*, 465–471. [[CrossRef](#)]
18. Diaconu, S.; Rusu, E. The Environmental Impact of a Wave Dragon Array Operating in the Black Sea. *Sci. World J.* **2013**, *2013*, 498013. [[CrossRef](#)]
19. Henderson, R. Design, simulation, and testing of a novel hydraulic power take-off system for the Pelamis wave energy converter. *Renew. Energy* **2006**, *31*, 271–283. [[CrossRef](#)]
20. Okoro, U.; Kolios, A.; Pérez-López, E.; Cui, L.; Sheng, Q. Wave Energy Converter System Safety Analysis. In Proceedings of the 11th European Wave and Tidal Energy Conference, Nantes, France, 6–11 September 2015.
21. Cornett, A.M. A global wave energy resource assessment. In Proceedings of the Eighteenth International Offshore and Polar Engineering Conference, Vancouver, BC, Canada, 6–11 July 2008.
22. Clément, A.; McCullen, P.; Falcão, A.; Fiorentino, A.; Gardner, F.; Hammarlund, K.; Lemonis, G.; Lewis, T.; Nielsen, K.; Petroncini, S.; et al. Wave energy in Europe: Current status and perspectives. *Renew. Sustain. Energy Rev.* **2002**, *6*, 405–431. [[CrossRef](#)]
23. Portillo, J.C.C.; Collins, K.M.; Gomes, R.P.F.; Henriques, J.C.C.; Gato, L.M.C.; Howey, B.D.; Hann, M.R.; Greaves, D.M.; Falcão, A.F.O. Wave energy converter physical model design and testing: The case of floating oscillating-water-columns—ScienceDirect. *Appl. Energy* **2020**, *278*, 115638. [[CrossRef](#)]
24. Cho, Y.H.; Nakamura, T.; Mizutani, N.; Lee, K.H. An Experimental Study of a Bottom-Hinged Wave Energy Converter with a Reflection Wall in Regular Waves—Focusing on Behavioral Characteristics. *Appl. Sci.* **2020**, *10*, 6734. [[CrossRef](#)]
25. Henfridsson, U.; Neimane, V.; Strand, K.; Kapper, R.; Bernhoff, H.; Danielsson, O.; Leijon, M.; Sundberg, J.; Thorburn, K.; Ericsson, E.; et al. Wave energy potential in the Baltic Sea and the Danish part of the North Sea, with reflections on the Skagerrak. *Renew. Energy* **2007**, *32*, 2069–2084. [[CrossRef](#)]
26. Gilloteaux, J.C.; Baba Rit, A.; Ducrozet, G.; Durand, M.; Clément, A. A Non-Linear Potential Model to Predict Large-Amplitudes-Motions: Application to the SEAREV Wave Energy Converter. In Proceedings of the ASME 2007 26th International Conference on Offshore Mechanics and Arctic Engineering, San Diego, CA, USA, 10–15 June 2007.
27. Pozzi, N.; Bracco, G.; Passione, B.; Sirigu, S.A.; Mattiazzo, G. PeWEC: Experimental validation of wave to PTO numerical model. *Ocean Eng.* **2018**, *167*, 114–129. [[CrossRef](#)]

28. Kanki, H.; Ariei, S.; Furusawa, T.; Otoyoy, T. Development of advanced wave power generation system by applying gyroscopic moment. In Proceedings of the 8th European Wave and Tidal Energy Conference, Uppsala, Sweden, 7–10 September 2009.
29. Genuardi, L.; Bracco, G.; Sirigu, S.A.; Bonfanti, M.; Paduano, B.; Dafnakis, P.; Mattiazzo, G. An application of model predictive control logic to inertial sea wave energy converter. In *Advances in Mechanism and Machine Science*; Springer: Cham, Switzerland, 2019.
30. Xu, J.; Yang, Y.; Hu, Y.; Xu, T.; Zhan, Y. MPPT Control of Hydraulic Power Take-Off for Wave Energy Converter on Artificial Breakwater. *J. Mar. Sci. Eng.* **2020**, *8*, 304. [[CrossRef](#)]
31. Amon, E.A.; Brekken, T.K.; Schacher, A.A. Maximum Power Point Tracking for Ocean Wave Energy Conversion. *IEEE Trans. Ind. Appl.* **2012**, *48*, 1079–1086. [[CrossRef](#)]
32. Mohammad, A.N.M.; Radzi, M.A.M.; Azis, N.; Shafie, S.; Zainuri, M.A.A.M. An Enhanced Adaptive Perturb and Observe Technique for Efficient Maximum Power Point Tracking Under Partial Shading Conditions. *Appl. Sci.* **2020**, *10*, 3912. [[CrossRef](#)]
33. Ahmed, J.; Salam, Z. A Modified P&O Maximum Power Point Tracking Method With Reduced Steady-State Oscillation and Improved Tracking Efficiency. *IEEE Trans. Sustain. Energy* **2016**, *7*, 1506–1515.
34. Zhang, F.; Thanapalan, K.; Procter, A.; Carr, S.; Maddy, J. Adaptive Hybrid Maximum Power Point Tracking Method for a Photovoltaic System. *IEEE Trans. Energy Convers.* **2013**, *28*, 353–360. [[CrossRef](#)]
35. Xiao, W.; Dunford, W.G. A modified adaptive hill climbing MPPT method for photovoltaic power systems. In Proceedings of the 2004 IEEE 35th Annual Power Electronics Specialists Conference (IEEE Cat. No.04CH37551), Aachen, Germany, 20–25 June 2004.
36. Na, W.; Chen, P.; Kim, J. An Improvement of a Fuzzy Logic-Controlled Maximum Power Point Tracking Algorithm for Photovoltaic Applications. *Appl. Sci.* **2017**, *7*, 326. [[CrossRef](#)]
37. Paz, F.; Ordonez, M. Ordonez, Zero Oscillation and Irradiance Slope Tracking for Photovoltaic MPPT. *IEEE Trans. Ind. Electron.* **2014**, *61*, 6138–6147. [[CrossRef](#)]
38. Kollimalla, S.K.; Mishra, M.K. Variable Perturbation Size Adaptive P&O MPPT Algorithm for Sudden Changes in Irradiance. *IEEE Trans. Sustain. Energy* **2014**, *5*, 718–728.
39. Killi, M.; Samanta, S. Modified Perturb and Observe MPPT Algorithm for Drift Avoidance in Photovoltaic Systems. *IEEE Trans. Ind. Electron.* **2015**, *62*, 5549–5559. [[CrossRef](#)]